



# AMERICAN METEOROLOGICAL SOCIETY

*Journal of Physical Oceanography*

## **EARLY ONLINE RELEASE**

This is a preliminary PDF of the author-produced manuscript that has been peer-reviewed and accepted for publication. Since it is being posted so soon after acceptance, it has not yet been copyedited, formatted, or processed by AMS Publications. This preliminary version of the manuscript may be downloaded, distributed, and cited, but please be aware that there will be visual differences and possibly some content differences between this version and the final published version.

The DOI for this manuscript is doi: 10.1175/JPO-D-14-0171.1

The final published version of this manuscript will replace the preliminary version at the above DOI once it is available.

If you would like to cite this EOR in a separate work, please use the following full citation:

Ascani, F., E. Firing, J. McCreary, P. Brandt, and R. Greatbatch, 2015: The deep equatorial ocean circulation in wind-forced numerical solutions. *J. Phys. Oceanogr.* doi:10.1175/JPO-D-14-0171.1, in press.



# The deep equatorial ocean circulation in wind-forced numerical solutions

5 François Ascani<sup>a,\*</sup>, Eric Firing<sup>b</sup>, Julian P. McCreary<sup>b,c</sup>,

Peter Brandt<sup>d</sup> and Richard J. Greatbatch<sup>d</sup>

10 <sup>a</sup> Marine Science Department, University of Hawaii at Hilo, 200 W. Kawili St., Hilo, HI 96720 USA

<sup>b</sup> School of Ocean and Earth Science and Technology, Department of Oceanography, University of  
Hawaii at Manoa, 1000 Pope Road, Honolulu, HI 96822 USA

<sup>c</sup> School of Ocean and Earth Science and Technology, International Pacific Research Center, University  
of Hawaii at Manoa, 1680 East-West Road, Honolulu, HI 96822 USA

15 <sup>d</sup> GEOMAR Helmholtz-Zentrum für Ozeanforschung Kiel, Kiel, Germany

20 *\*Corresponding author address:* François Ascani, Marine Science Department, University of Hawaii at  
Hilo, 200 W. Kawili St., Hilo, HI 96720 USA. E-mail: [fascani@hawaii.edu](mailto:fascani@hawaii.edu). Phone: 1-808-932-  
7575. Fax: 1-808-932-7588.

# Abstract

25        We perform eddy-resolving and high-vertical-resolution numerical simulations of the circulation in an idealized equatorial Atlantic Ocean in order to explore the formation of the deep equatorial circulation (DEC) in this basin. Unlike in previous studies, the deep equatorial intraseasonal variability (DEIV) that is believed to be the source of the DEC is generated internally by instabilities of the upper ocean currents.

30

Two main simulations are discussed: Solution 1, configured with a rectangular basin and with wind forcing that is zonally and temporally uniform; and Solution 2, with realistic coastlines and with an annual cycle of wind forcing varying zonally. Somewhat surprisingly, Solution 1 produces the more realistic DEC: The large-vertical-scale currents (Equatorial Intermediate Currents or EICs) are found  
35 over a large zonal portion of the basin, and the small-vertical-scale equatorial currents (Equatorial Deep Jets or EDJs) form low-frequency, quasi-resonant, baroclinic equatorial basin modes with phase propagating mostly downward, consistent with observations. We demonstrate that both types of currents arise from the rectification of DEIV, consistent with previous theories. We also find that the EDJs contribute to maintaining the EICs, suggesting that the nonlinear energy transfer is more complex  
40 than previously thought. In Solution 2, the DEC is unrealistically weak and less spatially coherent than in the first simulation probably because of its weaker DEIV. Using intermediate solutions, we find that the main reason for this weaker DEIV is the use of realistic coastlines in Solution 2. It remains to be determined, what needs to be modified or included to obtain a realistic DEC in the more realistic configuration.

# 1 Introduction

## 1.1 Overview

50        The equatorial Atlantic and Pacific Oceans exhibit a complex set of zonal currents at intermediate depths (500–2500 m), typically with an instantaneous amplitude of up to 15–25 cm/s (Fig. 1; Firing 1987; Schott *et al.* 1995, 2003; Firing *et al.* 1998; Gouriou *et al.* 1999, 2001; Bourlès *et al.* 2002, 2003; Send *et al.* 2002; Ollitrault *et al.* 2006; Eden and Dengler 2008; Ascani *et al.* 2010; Brandt *et al.* 2011, 2012; Cravatte *et al.* 2012; Youngs and Johnson 2014). This deep equatorial  
55        circulation (DEC; see a list of abbreviations in Tab. 1) is composed of two types of flow: Equatorial Deep Jets (EDJs), which are trapped on the equator and alternate with *depth* with a vertical wavelength of about 400–600 m; and Equatorial Intermediate Currents (EICs), which have a large vertical scale and alternate with *latitude* every 1–2° between about 5°S and 5°N<sup>1</sup>.

60        Both sets of currents contribute to the global ocean circulation and the zonal distribution of water masses and biogeochemical quantities. For instance, the eastward jets have been shown to supply dissolved oxygen to the oxygen minimum zone of the deep eastern equatorial Atlantic and Pacific Oceans (Stramma *et al.* 2005; Eden 2006; Brandt *et al.* 2008; Stramma *et al.* 2010; Czeschel *et al.* 2011; Brandt *et al.* 2012). Further, the large-scale biases in the nutrient and oxygen

---

<sup>1</sup> Latitudinally alternating large-vertical-scale zonal jets are also found at more poleward latitudes (see Ollitrault *et al.* 2006, Cravatte *et al.* 2012 and Qiu *et al.* 2013 for a recent account). We do not include them in the present paper but note that the dynamical similarity between these jets and the EICs is still unclear.

65 fields in global, coupled, biogeochemical ocean models have been attributed to inaccuracies of the simulated DEC (Dietze and Loeptien 2013; Getzlaff and Dietze 2013). Finally, Brandt *et al.* (2011) provide evidence that the upward-propagating energy and interannual variability of the EDJs in the Atlantic Ocean might be indirectly responsible for a portion of the interannual atmospheric variability *via* their modulation of sea surface temperature (SST).

70

On the modeling side, a realistic DEC is absent in most ocean general circulation model (OGCM) solutions. At the same time, recent theory and idealized numerical simulations have shown that the DEC may arise from the rectification of the deep equatorial intraseasonal variability (DEIV) (d'Orgeville *et al.* 2007; Hua *et al.* 2008; Ménesguen *et al.* 2009; Ascani *et al.* 2010). The reasons for  
75 this inconsistency are not clear. One possible cause is that DEIV, which arises internally from instabilities of the mean circulation in OGCMs, may be poorly reproduced in these models.

### *1.2 Present research*

80 In this study, we continue the effort to understand DEC dynamics and improve its modeling; for this purpose, we focus on the Atlantic Ocean. Specifically, we seek to reduce the gap between idealized and OGCM simulations by obtaining a series of numerical solutions that generate DEIV internally. We have tested many configurations with varying parameters and degrees of realism. Here, we focus on two: Solution 1, with a rectangular basin and with winds varying only with latitude; and Solution 2,  
85 with realistic coastlines and with an annual cycle of zonally and meridionally varying winds based on Atlantic climatology. We also briefly mention the results of two intermediate solutions (Solutions 1.5

and 1.8) to understand the differences between Solutions 1 and 2. In all solutions, instabilities of the upper-ocean mean equatorial circulation, known as Tropical Instability Waves (TIWs), provide the source for DEIV, and a DEC with some resemblance to Atlantic observations is obtained. Surprisingly, the more realistic DEC is obtained in the more idealized simulation (Solution 1): In particular, the EICs are found over a large zonal portion of the basin and the EDJs form low-frequency, quasi-resonant, baroclinic equatorial basin modes with phase propagating mostly downward, consistent with observations. We then study DEC dynamics by analyzing the zonal kinetic energy budget in Solution 1. We confirm the results of previous studies, that DEIV is the original source for DEC, but we also discover that the EDJs supply energy to the EICs, suggesting that the nonlinear energy transfer involved in the formation of DEC is more complex than previously assumed.

The paper is organized as follows. Section 2 provides a background for our study, reviewing the temporal and spatial characteristics of the EDJs and EICs in both the Pacific and Atlantic oceans, their simulation in previous idealized and realistic numerical models, and the theories proposed to explain them. Section 3 describes the overall design of our modeling experiments. Section 4 describes the upper-ocean circulation, DEIV, and DEC in Solutions 1 and 2, noting the similarity of the modeled EDJs to low-frequency, baroclinic equatorial basin modes. The results of the two intermediate solutions are also discussed. Section 5 discusses the dynamical processes that link DEIV to the DEC *via* the analysis of the zonal kinetic energy budget. Section 6 provides a summary and discussion of our results, including implications of the differences between Solutions 1 and 2 for the modeling of DEC in OGCMs.

## 2 Background

110

In this section, we review the temporal and spatial structure of observed EDJs and EICs, their reproduction in previous numerical models, and the theories proposed to explain them.

### 2.1 Observations

115

Multi-year collections of CTD and horizontal velocity data in the Atlantic Ocean provide information on the spatial and temporal characteristics of the EDJs and on their underlying dynamics. Johnson and Zhang (2003) analyzed the EDJ signature in the vertical strain of density from all available CTD data collected in the Atlantic Ocean, a dataset that spanned about 25 years. They  
120 concluded that the Atlantic EDJs have a period of about  $5\pm 1$  years and exhibit downward phase propagation; consistent with linear equatorial wave theory, the latter property implies upward energy propagation, suggesting that the origin of the EDJs lies in the deep ocean. These properties have been confirmed recently in an 8-year time series of horizontal velocity, obtained from moored measurements (reproduced here in Fig. 2a), from horizontal velocity observations spanning several decades derived  
125 from the net displacement of profiling floats (Brandt *et al.* 2011) and, more recently, from an extensive dataset of Argo and shipboard vertical density profiles (Youngs and Johnson 2015).

The relatively long period and small vertical wavelength of the EDJs are consistent with a dynamical description of the Atlantic EDJs in terms of quasi-resonant, low-frequency, baroclinic

130 equatorial basin modes (Cane and Moore 1981; d'Orgeville *et al.* 2007; Bunge *et al.* 2008; Brandt *et al.* 2011, 2012). These modes are composed principally of a Kelvin wave and its reflection into a first-meridional-mode long Rossby wave, with the period of the mode ( $T_n$ ) being a function of the gravity-wave phase speed of the particular baroclinic mode ( $c_n$ ),

$$T_n = \frac{4 L_B}{c_n}, \quad (1)$$

135

where  $L_B$  is the width of the basin. The smaller the vertical wavelength, the lower the gravity wave speed and, hence, the longer the period of the mode. For the Atlantic Ocean ( $L_B \sim 60^\circ$ ), the basin mode associated with vertical modes 14-16 ( $\sim 600$  m vertical wavelength;  $c_n \sim 20$  cm/s) has a period of about 4.2 years, which matches approximately the observed EDJ period. This dynamical interpretation in terms of basin modes is also consistent with the observed meridional structure of the EDJs (Johnson and Zhang 2003; Greatbatch *et al.* 2012).

In the Pacific Ocean, Firing (1987) observed the EDJs over a 16-month period and did not find any significant vertical migration. Johnson *et al.* (2002), however, analyzed the signature of the EDJs in the vertical strain of density in the Pacific Ocean, a dataset that spanned about 22 years. In the eastern Pacific, they found downward phase propagation at a rate suggesting a period of  $30 \pm 4$  years, but noted that inferring periodicity from this dataset is a “dangerous exercise”. In both Firing (1987) and Johnson *et al.* (2002), the EDJs corresponded to about vertical mode 32 ( $c_n \sim 10$  cm/s); with the Pacific Ocean being about  $140^\circ$  wide, a basin mode with this vertical scale should have a period of about 20 years, marginally less than the Johnson *et al.* (2002)'s estimate. Youngs and Johnson (2015)

150



recently analyzed an updated dataset, including 4 years of relatively dense sampling by high-resolution ARGO profiles in the Pacific. They found that the EDJ signal in the Pacific is much weaker in amplitude and broader in bandwidth than that in the Atlantic, making it more difficult to identify a single dominant periodic structure. Nevertheless, they isolated basin-scale zonal and temporal coherence  $1.5^\circ$  on either side of the equator centered at a vertical scale corresponding to mode 22 ( $c_n \sim 15$  cm/s). The phase propagation was downward and to the west, fitting a first-meridional-mode Rossby wave with a period of  $12 \pm 5$  years; for comparison, the period of a basin mode with the same vertical scale is 13 years<sup>2</sup>.

Unlike the EDJs, the EICs are *quasi-steady* zonal currents that have been observed consistently from direct velocity measurements (Firing 1987; Firing *et al.* 1998; Gouriou *et al.* 2001; Schott *et al.* 1998, 2003; Brandt *et al.* 2008) and from the displacements of floats (Ollitrault *et al.* 2006; Ascani *et al.* 2010; Cravatte *et al.* 2012; Ollitrault and Colin de Verdière 2014). Most prominently, they include (Fig. 1) a westward jet located on the equator, referred to in the literature as the Lower Equatorial Intermediate Current (LEIC); two eastward jets that flank the LEIC near  $1.5^\circ$ – $2^\circ$  from the equator, referred to as the North and South Intermediate Countercurrents (NICC and SICC); and a pair of westward jets,  $3$ – $4^\circ$  from the equator, the North and South Equatorial Intermediate Currents (NEIC and SEIC). Remarkably, the EICs extend across almost the entire width of the Atlantic and Pacific oceans (Fig. 3a).

## 2.2 Models

---

<sup>2</sup> Although zonal flows described as EDJs were initially observed in the Indian Ocean (Luyten and Swallow 1976), there have not been enough subsequent observations for a clear picture of EDJ behavior based on velocity profiles. From their analysis of vertical strain, Youngs and Johnson (2015) have inferred relatively weak EDJs with a 5-year period.

The EDJs are reproduced inconsistently in eddy-resolving ocean OGCMs of the Atlantic and Pacific oceans, partly, but not entirely, because of inadequate horizontal and vertical resolution (Ascani 2005; Eden and Dengler 2008). To our knowledge, they have been obtained only in one set of simulations of the Atlantic Ocean (Eden and Dengler 2008) and in the Pacific sector of the global simulation described by Ishida *et al.* (1998) (see Ascani 2005). In both cases, the modeled EDJs are associated with the instability of a deep cross-equatorial current along the western boundary, and their energy propagates *horizontally* into the interior *via* Kelvin waves with little or no reflection into long Rossby waves. Hence, unlike in the observations, they do not exhibit vertical propagation nor do they form low-frequency basin modes. With respect to the EICs, they are reproduced in numerical models with sufficient horizontal resolution, but they do not extend as deep as in the observations (Ascani 2005; Eden 2006; Ascani *et al.* 2010).

### 2.3 Theories

Hua *et al.* (2008) studied numerically and analytically the stability of a short<sup>3</sup> low-baroclinic-mode mixed Rossby-gravity (MRG) wave and showed how this wave can rectify into low-frequency motions resembling the EICs and the EDJs. The initial-value problem is addressed in the configuration of a long zonal channel; in this case, a zonally-confined packet of MRG waves destabilizes into EIC-like currents that propagate to the west and EDJ-like currents that propagate to the east of the packet. The vertical scale of the EDJs is a function of the zonal wavenumber (or, equivalently, the period) of the MRG wave, such that the shorter the wave, the longer its period and the shorter the vertical scale of

---

<sup>3</sup> Hereafter, 'short' refers to the zonal wavelength, and identifies Rossby waves with eastward group velocity and MRG waves with westward phase velocity.

the EDJs. For a zonal wavelength of about  $3^\circ$ , period of about 60 days, and wave amplitude of about 30  
195 cm/s, a stacked set of equatorial currents with a vertical wavelength of about 400 m is generated.

Hua *et al.* (2008) also studied the steady problem in the configuration of a basin with a MRG  
wave forced at the equator along the western boundary, a process mimicking the instabilities associated  
with the equatorial crossing of the deep western boundary current (DWBC) in the Atlantic Ocean. In  
200 this case (which is more thoroughly studied by d'Orgeville *et al.* 2007), EDJ-like currents are also  
generated, propagating into the interior and forming low-frequency equatorial basin modes. In this  
scenario, the vertical scale of the EDJs does not depend on the basin width, so the appearance of the  
EDJs as basin modes does not appear to be essential to the theory. EIC-like currents also appear but  
only within a few degrees from the western boundary, inconsistent with the Atlantic observations.

205

To remedy this discrepancy, Ménesguen *et al.* (2009) explore the case where the forcing is still  
along the western boundary but is now confined to the upper 2500 m – instead of appearing as a single  
baroclinic mode. In this case, the forcing excites not only the short low-baroclinic-mode MRG waves  
but also short barotropic equatorial Rossby waves. The MRG waves generate EDJs which form basin  
210 modes, while the short barotropic Rossby waves generate EICs over a large zonal portion of the basin,  
as in the observations.

The scenario of d'Orgeville *et al.* (2007) and Ménesguen *et al.* (2009), schematized in Fig. 4a, is  
appealing in that it reproduces currents resembling EDJs and EICs in structure and amplitude and that  
215 the EDJs form basin modes. One difference from the observations, however, concerns the observed  
vertical propagation of the EDJs: The phase of the EDJs propagates both upward and downward in the

simulation of d'Orgeville *et al.* (2007) while it propagates dominantly downward in the observations (Fig. 2a). Another issue concerns the zonal extent of the EICs, which depends critically on how far the short barotropic Rossby waves can propagate into the interior ocean before they become unstable and  
220 lose their energy to the EICs. Although the decay might not pose a problem for the narrower Atlantic Ocean, it does for the broader Pacific: For the short Rossby waves to cover a large fraction of the Pacific basin before becoming unstable, they would have to be very weak, in which case little energy is available for generating basin-wide EICs.

225 A second scenario for producing EICs over a long zonal extent has been proposed by Ascani *et al.* (2010). Instead of DEIV being generated along the western boundary by instabilities of a DWBC, Ascani *et al.* (2010) propose that the DEIV is generated by the instabilities of the upper-ocean equatorial current system, in particular those associated with TIWs (Fig. 4b). As seen in the realistic simulation analyzed by von Schuckmann *et al.* (2008) and in the observations and realistic simulations  
230 reviewed by Ascani *et al.* (2010), a large fraction of TIW energy radiates into the deep ocean as a downward- and eastward-propagating beam of monthly-periodic MRG waves. Fig. 3b presents new evidence for this with a map of the mean eddy kinetic energy (EKE) near 1000 m, determined from the meridional velocity component ( $v$ ) estimated from Argo float displacements (see Ollitrault and Colin de Verdière 2014); because near-equatorial  $v$  naturally peaks in the intraseasonal wave band, the plot  
235 indicates enhanced DEIV along the equator, especially in the eastern Pacific Ocean and western Atlantic Ocean where the TIW-generated MRG waves are expected (blue frames in Fig. 3b). Ascani *et al.* (2010) use surface forcing to generate an idealized beam of MRG waves in their numerical model. When the MRG waves are weak, a set of Eulerian mean currents resembling the EICs appear but they are confined zonally within the beam and the associated Lagrangian mean currents are everywhere

240 zero; when the MRG waves are strong, the EIC-like Eulerian mean currents are found within and to the west of the beam, extending to the western boundary, and they are associated with non-zero Lagrangian mean currents<sup>4</sup>.

The dynamical interpretation of these results given by Ascani *et al.* (2010) differs substantially  
245 from Hua *et al.* (2008)'s theory. Ascani *et al.* (2010) identified two types of wave instability. The first instability is the *self-interaction* of the MRG waves (a process neglected in Hua *et al.* 2008) which gives rise to EIC-like currents within the beam (but not outside). Due to the second instability, the MRG waves lose energy to other types of wave; its main role is to cascade the energy of the MRG wave toward small vertical scales where it is dissipated. Unlike in Hua *et al.* (2008)'s scenario, the  
250 dissipation is key here because it alters potential vorticity at depth and enables the EIC-like currents resulting from the self-interaction to extend west of the beam, a process that is dynamically similar to the formation of a  $\beta$ -plume circulation (Stommel 1982, Pedlosky 1996; Kessler *et al.* 2003). Under this scenario, the EICs can be found over a very long zonal scale even if the MRG wave activity is itself zonally confined. We should also note that the focus differs between Hua *et al.* (2008) and Ascani *et al.*  
255 (2010); in the former, the focus is on the *initial-value* problem while, in the latter, it is on the *statistically steady state* problem. Despite these differences, however, both studies involve a transfer of energy from DEIV to EICs, and this is the fundamental property that we will check while studying the dynamics of EICs in our solutions (section 5.2).

---

4 Although the distinction between Eulerian and Lagrangian mean of the circulation is dynamically important (and central to understanding the effects of these currents on the distribution of tracers), the present work is concerned principally with the Eulerian mean. See Ascani *et al.* (2010) for a thorough discussion of the Lagrangian mean associated with the EICs.

### 3 Experimental design

260

Our ocean model is a version of the Parallel Ocean Program (POP 2.0) model (*e.g.*, Maltrud and McClean 2005), extending from 20°S to 20°N and from 58°W to 14°E to approximate the width of the equatorial Atlantic Ocean, and with a flat bottom at 5000 m. Its horizontal resolution is 1/4° in both longitude and latitude and it has 100 levels, with the vertical resolution progressively decreasing from  
265 10 m near the surface to 100 m near the bottom. Horizontal mixing is parameterized by biharmonic viscosity and diffusion with a coefficient of  $-2 \times 10^{10} \text{ m}^4/\text{s}$ , and vertical mixing follows the Richardson-number-dependent scheme of Pacanowski and Philander (1981) with a background diffusivity of  $10^{-5} \text{ m}^2/\text{s}$ . We use a free-slip bottom boundary condition because preliminary experiments showed that  
270 quadratic bottom drag with a non-dimensional drag coefficient of  $1.225 \times 10^{-3}$  reduces the DEIV barotropic energy by more than half, thereby significantly reducing the energy source for DEC (see section 6.3).

We obtain four solutions (Tab. 2). The first (Solution 1) is obtained in the rectangular basin noted above. It is forced over the whole domain by the zonal and time-averaged winds observed over  
275 the Atlantic Ocean from the European Remote Sensing (ERS-1/2) scatterometer product; hence, the wind stress does not vary in longitude and time but has a realistic meridional profile. The second (Solution 2) has the same configuration as Solution 1, except that it is configured with a realistic coastline of the equatorial Atlantic Ocean (but still with vertical walls at the boundaries), and it is forced by the zonally, meridionally and monthly-varying ERS-1/2 wind stress climatology. The first  
280 intermediate solution (Solution 1.5) is similar to Solution 1 except that it has a realistic coastline. The second intermediate solution (Solution 1.8) differs from Solution 2 only in having annual-mean winds

(no annual cycle).

Sponge layers were not used in these simulations. Experiments including sponge layers on the northern and southern boundaries, implemented *via* Rayleigh damping, yielded EDJ basin modes but reduced their amplitude by half. This was apparently an indirect effect *via* reduction of the DEIV, because in the simulations without sponge layers the high vertical mode coastal Kelvin wave energy does not reach the zonal boundaries, so it would be unaffected by sponge layers there.

The simulations are spun up from a state of rest. Temperature is initially horizontally uniform with a vertical profile derived from the observed potential temperature averaged zonally and meridionally within 5° of the equator in the Atlantic (World Ocean Atlas 2001), and surface temperature is relaxed to the climatological mean with a time scale of one month. Salinity is uniform at 35 throughout each simulation, a simplification that is acceptable for our purpose. The integrations span 50 years for Solution 1, 30 years for Solution 2, 9 years for Solution 1.5 and 15 years for Solution 1.8. Five-day averages are archived in all years for Solution 1 and in years 24–29 for Solution 2. (Five-day averages and snapshots are nearly identical.) One-year means are archived for all years for Solutions 1.5 and 1.8.

## 4 Model Results

In this section, we report relevant aspects of the flow fields of Solutions 1 and 2, describing first their upper-ocean circulation and DEIV (section 4.1) and then their deep zonal currents that resemble the DEC (section 4.2). We continue by presenting evidence that the spatial and temporal structure of the modeled EDJs in Solution 1 matches that of quasi-resonant, low-frequency, baroclinic equatorial basin modes (section 4.3). We conclude with a brief description of the two intermediate solutions (Solutions 1.5 and 1.8) to help to understand the differences between Solutions 1 and 2.

#### 4.1 Upper-ocean circulation and DEIV

Fig. 5 shows the 5-year mean, near-surface, zonal current and EKE from observations (top panels) and in Solutions 1 and 2 (middle and bottom panels, respectively). The South Equatorial Current (SEC), the North Equatorial Countercurrent (NECC), and a fraction of the North Brazil Current (NBC) are well reproduced in Solution 2 (panel e). In Solution 1 (panel c), the NECC is about 50% stronger than observed mostly because the zonal width of the basin in Solution 1 is larger than in the observations (see section 4.4). The western boundary current is purely meridional, so there is no zonal component corresponding to the NBC.

The surface EKE field in Solution 2 is overall more realistic than in Solution 1. The high EKE region along the NECC in Solution 2, however, is larger in amplitude but smaller in zonal extent than in the observations. In Solution 1, the high EKE region is stronger and more zonal than in the observations but its zonal extent matches the observations.

The DEIV in Solution 1 (Fig. 6) is similar to that in Solution 2, but stronger in amplitude



(Fig. 7). It is composed of large-vertical-scale Rossby waves with short periods (30–100 days), moderate meridional scale ( $\sim 10^\circ$ ) and moderately short zonal wavelengths ( $5\text{--}8^\circ$ ) (Figs. 6c and e). Near the equator, it includes MRG waves with zonal wavelength of about  $8^\circ$  that are distributed over a range of vertical modes, with higher vertical modes corresponding to lower frequencies (Figs. 6d and  
330 f). The increase in small vertical scale energy on the equator is clearly visible in the time series of the meridional velocity component ( $v$ ) at  $23^\circ\text{W}$ ,  $5^\circ\text{N}$  and  $23^\circ\text{W}$ ,  $0^\circ\text{N}$  (Figs. 6a and b). Based on the analysis of a realistic simulation by von Schuckmann *et al.* (2008), we conclude that the large-vertical-scale waves of the DEIV correspond to the deep signature of TIWs and are forced by the instability of the upper-ocean circulation. With respect to the moderate- to high-vertical-mode MRG waves at the  
335 equator, we will see in section 5.3 that they result instead from the formation mechanism that gives rise to the EDJs.

Spectra of  $v$ , zonally- and vertically-averaged along the equator (Fig. 7), are similar in shape for the two solutions, but are weaker by a factor of about 3 in Solution 2, consistent with the weaker upper-  
340 ocean circulation in this run (Fig. 5). Using the velocity observations described by von Schuckmann *et al.* (2008), we compare observed and modeled equatorial  $v$  at  $23^\circ\text{W}$  using spectra calculated at every available depth between the surface and 700 m (Fig. 8). As already shown by von Schuckmann *et al.* (2008; their Fig. 3), there is an increase in DEIV for periods of 20-50 days between 100 and 300 m depth. A similar feature is seen in Solution 2, and a more energetic version appears in Solution  
345 1. In both simulations, the DEIV energy elevation appears to extend deeper than in these observations. Model-data comparisons of spectra of equatorial  $v$  are also performed using four additional datasets: the velocity measurements described by Bunge *et al.* (2008) at  $23^\circ\text{W}$  between 600 and 1500 m depth and at  $10^\circ\text{W}$  between 750 and 1700 m depth as well as the velocity observations collected during the

World Ocean Circulation Experiment at 36°W between 3000 and 4000 m depth (Mooring ACM10) and  
350 14.5°W between 1500 and 3000 m depth (Mooring ACM11)<sup>5</sup>. According to these comparisons, the  
intraseasonal meridional velocity in both simulations appears to be comparable to the observations  
above about 1500 m depth but is larger than in the observations by a factor of 3-4 below that depth  
(Fig. 9). Error bars are large, however, so it is not clear which solution reproduces a more realistic  
DEIV. Note also that both simulations lack energy at lower frequencies, especially at the two  
355 easternmost locations.

The Argo-derived meridional velocity components near 1000 m (Fig. 10) provide an estimate of  
the *horizontal* distribution of DEIV energy along the equator. At this depth, Solution 1 reproduces the  
increase in EKE all along the equator (within 3-4°) although it appears to somewhat overestimate its  
360 magnitude. In Solution 2, however, the increase in EKE along the equator is much weaker. Quantitative  
comparison to Argo is not yet possible, given the available sampling.

In conclusion, it is not clear which of the two solutions reproduces a more realistic DEIV; it  
might be that Solution 2 is more realistic over the depth range where the DEIV is the largest (upper  
365 300 m; Fig. 8) but less so below at intermediate depths where the DEC is generated. Furthermore, this  
comparison to observations is hampered by severe undersampling, so that it is restricted to localized  
comparisons of energy level.

#### 370 4.2 Deep zonal currents

5-day averages, 6-month averages and 5-year averages of the zonal current along 34°W in the

---

5 Data along with references can be found at  
[http://www.nodc.noaa.gov/woce/woce\\_v3/wocedata\\_1/cmdac/netcdf/explist.htm](http://www.nodc.noaa.gov/woce/woce_v3/wocedata_1/cmdac/netcdf/explist.htm).

simulations are shown in Fig. 11. In both runs, the 5-year mean circulation is dominated by a set of large-vertical-scale flows spanning the whole water column and alternating with latitude. The three  
375 flows nearest the equator resemble the EICs described in section 2. They are, however, much more realistic in Solution 1 than in Solution 2: In Solution 1, they attain current speeds of 5–10 cm/s and extend over nearly 40° longitude in the western half of the basin (Fig. 12), consistent with the observations, while in Solution 2 their amplitude is only half as great and they are much less zonally coherent.

380

The 6-month mean in both solutions has a set of small-vertical-scale currents at the equator (Fig. 11, middle panels). In Solution 1, the set of equatorial currents resembles the observed EDJs, with an amplitude reaching 10 cm/s; the vertical wavelength is about 1000 m, compared to about 600 m in the Atlantic. Consistent with quasi-synoptic observations (Fig. 1), the EDJs in Solution 1 appear also in  
385 5-day averages with an amplitude reaching 20 cm/s (Fig. 11, left panels). In Solution 2, however, the set of equatorial currents does not have a well-defined vertical wavelength and its amplitude reaches only a few cm/s, even in 5-day averages; it is unclear whether this set should be considered as a reasonable, albeit weak, reproduction of the EDJs.

390 The modeled EDJs in Solution 1 are the most realistic reported so far in the literature, varying in time and depth in a fashion remarkably similar to the observations at 23°W, 0°N (Fig. 2b). Fig. 13 provides a depth-time plot of the low-frequency, zonal velocity ( $u$ ) at 23°W in Solution 1 (the quantity is scaled and the vertical coordinate stretched with a reference buoyancy frequency of 1 cph; Gill 1982). Like the observed EDJs, phase propagates downward and their energy upward, with a  
395 period of several years. Although both downward and upward energy propagation occurs within the

first 12 years of the run (not shown), the rest of the simulation is dominated by upward energy propagation, with a modulation at the decadal time scale (Fig. 13).

### 4.3 Basin modes

400

In agreement with the observations, the EDJs in Solution 1 have properties consistent with their being the equatorial expressions of quasi-resonant, low-frequency, baroclinic, equatorial basin modes (section 2). The frequency-vertical wavenumber spectrum (Fig. 14) shows that zonal kinetic energy on the equator is concentrated near the basin-mode prediction (1), with a preponderance of upward energy  
405 propagation. The lack of symmetry between downward and upward energy propagation suggests that the modes are energized at depth and dissipated nearer the thermocline; the upward-going energy decays to low values before reaching 300 m, and there is little or no energy descending from the 300-m level (Fig. 13). The energy of the basin modes is centered around vertical mode 12 and spans vertical modes 6 to 17. The observed Atlantic EDJs have their energy centered on vertical mode 15 and spread  
410 over vertical modes 12 to 20 (Brandt *et al.* 2008) so that the modeled EDJs in the run with idealized forcing correspond to somewhat larger vertical scales and shorter periods.

The spatio-temporal structure of the low-frequency  $u$  and pressure fields in Solution 1 resembles that of basin modes. The similarity is illustrated in Fig. 15, which presents maps of  $u$   
415 associated with upward-propagating energy for the stretched vertical wavelength of 930 m (vertical mode 12) with a resonant period of 3.9 years. To fit the analytical solution from the theory of Cane and Moore (1981) to the numerical one, we used a Rayleigh damping coefficient  $r(l) = |l|r_o$ , where  $r_o = 2 \times 10^{-9} \text{ s}^{-1}$ , which increases linearly with the absolute meridional mode number  $|l|$  to mimic the scale-

dependent, biharmonic dissipation used in the numerical model<sup>6</sup>. We calculate the solution by summing  
 420 over all odd meridional mode numbers between -1 and 51; this is a sufficient number of modes as about  
 90% of the variance is explained solely by the sum of the Kelvin wave ( $l=-1$ ) and first-meridional  
 mode Rossby wave ( $l=1$ ). Differences between the numerical and analytical solution occur mainly at  
 20°W; at this longitude, the meridional width of the pattern is smaller in the analytical solution than in  
 the numerical one, and there are phase differences between the two solutions on and off the equator.  
 425 Despite these differences, the comparison in Fig. 15 supports the interpretation of the EDJs in Solution  
 1 as being the sum of low-frequency baroclinic equatorial basin modes<sup>7</sup>.

In Solution 2, the zonal motion along the equator is dominated by annual and semi-annual  
 waves with low vertical wavenumbers and with net downward propagation of energy (Fig. 14b). The  
 430 annual peaks occur at wavenumbers consistent with basin modes, as seen in previous numerical studies  
 (Thierry *et al.* 2004). At lower frequencies, there is a weak local peak of upward-propagating energy  
 that lies on the basin mode dispersion curve, with about the same moderately high vertical  
 wavenumbers ( $0.9-1.2 \times 10^{-3}$  cycles-per-meter) and frequencies ( $1/8-1/2$  cycles-per-year) as in Solution  
 1; however, the signal is no larger than other weak local peaks that are not on the basin-mode curve,  
 435 consistent with the lack of a clear EDJ signal in the time series of equatorial  $u$  of Fig. 2c or in the  
 6-month mean of Fig. 11e.

---

6 Although Rayleigh damping is not directly comparable to the Laplacian dissipation used in Greatbatch *et al.* (2012) to fit a numerical solution of the EDJ-like basin modes to observations, the magnitude of the damping used here appears somewhat weaker. Using Greatbatch *et al.* (2012)'s notation, if we assume that dissipation in their model is controlled by  $A\partial_{yy}$ , then  $r$  is equivalent to  $A/L_y^2$  where  $L_y$  is a meridional scale. With  $A=300$  m<sup>2</sup>/s and  $L_y=100$  km,  $A/L_y^2$  is  $3.10^{-8}$  s<sup>-1</sup>. This discrepancy can be explained in part by the region and the criterion chosen for fitting: here we use three longitudes and compare the shape of their  $y-t$  patterns while in Greatbatch *et al.* (2012) the region between 30°W and 15°W is used and the fitting is based on the meridional width of the EDJs.

7 Consistent with this conclusion, we have also checked that little energy is cycling back to the western boundary *via* Kelvin waves along the northern and southern boundaries.

#### 4.4 Intermediate solutions

440           Finally, we conclude with a brief description of the two intermediate Solutions 1.5 and 1.8. Both are closer to Solution 2 than to Solution 1 indicating that the differences between Solution 1 and 2 are mostly due to the change in coastline rather a change in wind stress.

          The upper-ocean circulation in Solutions 1.5 and 1.8 is similar to that in Solution 2 (not shown).  
445   In particular, the maximum speeds of the upper-ocean currents near the western boundary are reduced and reach the realistic level obtained in Solution 2 once a realistic coastline is used. This is because the maximum amplitude of these currents is controlled mostly by the Sverdrup balance and depends on the zonal length over which the wind stress curl is integrated; with a reduced basin in the zonal direction once the realistic coastline is introduced, the maximum speed of the circulation is reduced as well.  
450   Consequently, the upper-ocean circulation is less unstable in the two intermediate solutions compared to Solution 1 and their DEIV has a magnitude similar to that in Solution 2. The DEC in Solutions 1.5 and 1.8 is also similar in shape and amplitude to the DEC in Solution 2 (not shown). One noticeable difference between Solutions 1.5, Solution 1.8 and Solution 2, however, is that the EICs become weaker and less spatially coherent going from Solution 1.5 to Solution 1.8 to Solution 2 (not shown);  
455   this suggests that some aspect of the DEC are sensitive to the zonal structure and annual cycle of the wind stress.

## 5 Dynamical Interpretation

460 In section 4, we discussed basic properties of Solutions 1 and 2, among other things noting that they contain high-frequency energy (DEIV) and low-frequency structure (DEC). Here, we study the formation mechanism of the most realistic DEC (Solution 1). To do so, we develop an analysis of the zonal kinetic energy budget in the frequency and wavenumber domain, using stretched vertical coordinate (section 5.1). This approach enables us to identify the set of nonlinear interactions among  
465 individual waves in the DEIV that produce the LEIC (section 5.2) and EDJs (section 5.3) in Solution 1<sup>8</sup>.

### *5.1 The zonal kinetic energy budget in frequency-vertical wavenumber space*

470 The zonal momentum equation at the equator is

$$u_t = -(u u_x + v u_y + w u_z) - \frac{1}{\rho_0} p_x + D_H^x + D_V^x, \quad (2)$$

where subscripts represent partial derivatives,  $u$ ,  $v$ , and  $w$  are the zonal, meridional and vertical components of the velocity field,  $p$  is pressure,  $\rho_0$  is a constant reference density, and  $D_H^x$  and  $D_V^x$  are  
475 the zonal components of the horizontal and vertical viscous terms, respectively. Following Saltzman (1957), Eq. (2) is Fourier transformed in frequency-vertical wavenumber space:

---

<sup>8</sup> Although the Liouville-Green (also known as WKB) approximation used for scaling and stretching the dynamical quantities is not strictly valid for the large-vertical-scale MRG waves, it is used here simply as a rough scale separation mechanism and does not affect our interpretation concerning the nonlinear interactions.

$$i(2\pi f)\hat{u} = -(\widehat{u}u_x + \widehat{v}u_y + \widehat{w}u_z) - \frac{1}{\rho_0}\widehat{p}_x + \widehat{D}_H^x + \widehat{D}_V^x, \quad (3)$$

where the hat represents the Fourier-transform operator and each quantity is a function of frequency  $f$  (in cycles per unit of time), wavenumber  $m$  in *stretched* vertical coordinate (in cycles per unit of stretched length), longitude  $x$ , and latitude  $y$ . We choose to represent the depth-time dependence as  $\exp(2\pi i(m_0 z + f_0 t))$  so that  $m_0 > 0$  and  $f_0 > 0$  correspond to a *downward phase* and *upward energy* propagating signal. The zonal component of the kinetic energy equation in the frequency-vertical wavenumber space is thus

485

$$i(2\pi f)\hat{u}^* \hat{u} = -\hat{u}^* (\widehat{u}u_x + \widehat{v}u_y + \widehat{w}u_z) - \hat{u}^* \frac{1}{\rho_0}\widehat{p}_x + \hat{u}^* \widehat{D}_H^x + \hat{u}^* \widehat{D}_V^x, \quad (4)$$

where the asterisk denotes the complex conjugate. The left hand side of Eq. (4) is imaginary, so the real parts of the terms on the right hand side sum to zero with their relative magnitudes indicating how the “zonal” kinetic energy,  $u^2$ , is generated and dissipated (Hayashi, 1982). Calculating these terms for the equatorial slice below 300 m, we find a good numerical balance between the positive and negative contributions in Eq. (4) (Figs. 15a and b, respectively) for all frequencies and vertical wavenumbers. (A weak term,  $\hat{u}^* \cdot \widehat{D}_H^x$ , is not shown.) Next, this energy balance is used to infer the relationships among the DEIV, the LEIC, and the EDJs.

## 495      5.2 Linkage of DEIV to LEIC

The LEIC is a time-mean flow with a large vertical scale, so it corresponds to the region of Fig. 16 near zero frequency and zero vertical wavenumber (small square in Fig. 16a). The two terms that perform positive work are the meridional and zonal advective terms ( $-vu_y$  of Fig. 16a and  $-uu_x$  of Fig. 16c, respectively), while the energy loss is mainly *via* the vertical advective term and zonal pressure gradient term ( $-wu_z$  of Fig. 16d and  $-p_x/\rho_0$  of 16e, respectively). To identify the nonlinear wave



interactions that contribute to the maintenance of the LEIC against dissipation, we look at all pairs of waves  $(f_1, m_1)$  and  $(f_2, m_2)$  that contribute to the motion at  $(f_0, m_0) = (0, 0)$  via the terms  $-vu_y$  and  $-uu_x$ , where  $f_1 + f_2 = f_0$  and  $m_1 + m_2 = m_0$ . In the frequency-vertical wavenumber space, that means we look at

505

$$-\hat{u}^*(f_0, m_0) \hat{v}(f_1, m_1) \hat{u}_y(f_2, m_2) - \hat{u}^*(f_0, m_0) \hat{v}(f_2, m_2) \hat{u}_y(f_1, m_1) \quad (5)$$

for  $-vu_y$ , and

$$-\hat{u}^*(f_0, m_0) \hat{u}(f_1, m_1) \hat{u}_x(f_2, m_2) - \hat{u}^*(f_0, m_0) \hat{u}(f_2, m_2) \hat{u}_x(f_1, m_1). \quad (6)$$

510 for  $-uu_x$ . Note that, for each expression, the first term is symmetric to the second one with respect to rotation around the point  $(f_0/2, m_0/2)$ . For the LEIC,  $(f_0, m_0) = (0, 0)$ ,  $f_1 = -f_2$ ,  $m_1 = -m_2$ , and the two terms in each expression are equal.

Quantities in (5) and (6) for  $(f_0, m_0) = (0, 0)$  are plotted in Figs. 17 and 18, respectively. First, we  
 515 find that the energy transfer via  $-vu_y$  results from the interaction of high-frequency waves (mostly short Rossby waves with frequencies from 1/100 to 1/50 cycles-per-day) that are of large vertical scale (Fig. 17). This is consistent with the general mechanism proposed by Hua *et al.* (2008) and Ascani *et al.* (2010), that DEIV is one important source for the EICs via a transfer of energy from high-frequency waves to the EICs<sup>9</sup>. Second, and quite unexpectedly, we also find an energy transfer from low-  
 520 frequency baroclinic equatorial basin modes, corresponding to EDJs, to the LEIC via the  $-uu_x$  term (Fig. 18); the interpretation is that each basin mode interacts with itself to transfer energy to the zero-

---

<sup>9</sup> Although in Ascani *et al.* (2010), the high-frequency waves involved in the transfer have a vertical wavelength ( $\sim 1700$  m) smaller than those involved here, the transfer is *not* dependent on this vertical scale as the self-interaction of a wave field of any vertical wavelength produces a large-vertical-scale mean flow.

frequency and zero-vertical-wavenumber component that corresponds to the LEIC. To check this result, we calculate the same work but in *physical space*, that is,

$$U^{EIC} \cdot \langle -u^{EDJ} u_x^{EDJ} \rangle, \quad (7)$$

525

where  $U^{EIC}$  is the time-mean zonal velocity vertically averaged below 300 m,  $u^{EDJ}$  is the zonal velocity field associated with one particular basin mode, (shown in Fig. 15) and the angle brackets indicate a time and vertical mean. In the western half of the basin, quantity (7) is positive on the equator and negative  $2^\circ$  on either side of it (Fig. 19) confirming that the EDJs tend to accelerate the LEIC (consistent with Fig. 18) and decelerate the NICC and SICC. This suggests that, in the statistically steady state, the transfer of energy that maintains the EICs is more complex than initially described by Hua *et al.* (2008) and Ascani *et al.* (2010) and involves not only a transfer from high- to low-frequency components but also *between* low-frequency components.

535

### 5.3 Linkage of DEIV to EDJs

All motions corresponding to the EDJs (dotted lines in Fig. 16) are maintained solely *via* the meridional advective term  $-vu_y$ , while energy loss is *via* the zonal advective term, the zonal pressure gradient term and the vertical friction term ( $-uu_x$  of Fig. 16c,  $-p_x/\rho_0$  of 16e and  $D_v^x$  of 16f, respectively). As for the LEIC, we identify the pairs of waves that contribute to a specific basin mode  $(f_0, m_0)$  *via* the term  $-vu_y$  using expression (5), but two additional steps are performed initially. In the first step, we distinguish between the eastward- (Kelvin wave) and westward-propagating (long Rossby wave) components of the basin mode. Hence, the contribution to the Kelvin-wave component of the basin

540

mode is

545

$$-\hat{u}^*(f_0, m_0; E) \hat{v}(f_1, m_1) \hat{u}_y(f_2, m_2) - \hat{u}^*(f_0, m_0; E) \hat{v}(f_2, m_2) \hat{u}_y(f_1, m_1), \quad (8)$$

and that to the Rossby-wave component of the basin mode is

$$-\hat{u}^*(f_0, m_0; W) \hat{v}(f_1, m_1) \hat{u}_y(f_2, m_2) - \hat{u}^*(f_0, m_0; W) \hat{v}(f_2, m_2) \hat{u}_y(f_1, m_1), \quad (9)$$

550 where  $\hat{q}(f_i, m_i; E)$  and  $\hat{q}(f_i, m_i; W)$  are the Fourier components of  $q$  at the frequency  $f_i$  and vertical wavenumber  $m_i$  with eastward (E) and westward (W) phase propagation, respectively. In the second step, we focus on wave pairs composed of waves with westward-propagating phase only; this reduces the noise in the calculation without changing the pattern. Hence, quantities (8) and (9) become (10) and (11), respectively:

555

$$-\hat{u}^*(f_0, m_0; E) \hat{v}(f_1, m_1; W) \hat{u}_y(f_2, m_2; W) - \hat{u}^*(f_0, m_0; E) \hat{v}(f_2, m_2; W) \hat{u}_y(f_1, m_1; W), \quad (10)$$

and

$$-\hat{u}^*(f_0, m_0; W) \hat{v}(f_1, m_1; W) \hat{u}_y(f_2, m_2; W) - \hat{u}^*(f_0, m_0; W) \hat{v}(f_2, m_2; W) \hat{u}_y(f_1, m_1; W). \quad (11)$$

Quantities (10) and (11) are plotted in Fig. 20 for the (upward-energy) basin mode with  
560  $m_0=1/645$  cycles-per-meter and the associated resonant frequency  $f_0=1/5.5$  cycles-per-year (circle symbol in Fig. 16a); results are qualitatively similar for other upward-energy basin modes. The plot

demonstrates that the  $(f_0, m_0)$  motion is generated (red/yellow regions) from pairs of MRG waves that range in frequency from 1/100 to 1/30 cycles-per-day, with one wave having a low vertical wavenumber and the other having a vertical wavenumber close to  $m_0$ ; these are the two types of high-frequency waves that were described in section 4.1 and Fig 6. Note that the intraseasonal high-vertical-wavenumber energy arises *in situ* as part of the interactions, while the low-vertical-wavenumber energy corresponds to TIWs and arises from remote instability of surface equatorial currents<sup>10</sup>. Further, the interactions between the two types of high-frequency waves contribute to both the Kelvin- and Rossby-wave components of the basin mode, with the interaction for the latter being somewhat stronger.

The aforementioned properties are generally consistent with the theory of Hua *et al.* (2008) for the EDJs. One difference, however, is that Hua *et al.* (2008) found that a MRG wave with a specific period gives rise to the EDJs at a specific vertical wavenumber, whereas in our solution all MRG waves (from 30 to 100-day period) participate in the generation of any specified vertical mode. Another is that in Hua *et al.* (2008), MRG destabilization only generates the Kelvin-wave component of high vertical mode basin modes, whereas we find that, here, it energizes both the Kelvin- and long-Rossby-wave components. Hence, as for EICs, the nonlinear transfer of energy toward EDJs in the statistically steady state appears to be more complex than the transfer described in the initial-value problem studied by Hua *et al.* (2008).

To address the issue of the asymmetry between upward- and downward-energy basin modes, we repeated the above analysis but for a downward-energy basin mode. Quantities (10) and (11) are found weaker by an order of magnitude than in the upward-energy case over all frequencies and vertical wavenumbers (not shown). This likely results from the weakness of the downward-energy

<sup>10</sup> In the ocean, intraseasonal high-vertical-wavenumber energy also arises directly from the instability of the surface equatorial currents (e.g. von Schuckmann *et al.* 2008) but this is somewhat underestimated in our model.

585 basin mode itself and, unfortunately, does not provide an explanation of why this is the case.

Finally, and for completeness, we also looked at the pair of waves that contribute to the dissipation of the (upward-energy) EDJs via the term  $-uu_x$ . In contrast with the LEIC case, however, we found no pattern in the frequency-vertical wavenumber space (not shown).

590

## 6 Conclusions

### *6.1 Summary*

595 The present study is an attempt to reproduce the DEC in a more realistic setting than in previous studies. In particular, instead of directly exciting a particular set of intraseasonal waves, the approach followed here is to let these waves arise from the instabilities of the large-scale circulation.

600 The DEC obtained in Solution 1 (rectangular basin and steady wind forcing) has some realistic features. In particular, the EICs extend over a large zonal portion of the basin while the EDJs form low-frequency quasi-resonant equatorial basin modes with energy propagating upward, consistent with the observations.

Further analyses of this simulation confirm the conclusion of previous studies that the DEC

605 results from the rectification of DEIV. In particular, we show that the maintenance of both the EDJs and the EICs is consistent with the instability and nonlinear modification of intraseasonal MRG and Rossby waves, as discussed by previous investigators (d'Orgeville *et al.* 2007; Hua *et al.* 2008; Ménesguen *et al.* 2009; Ascani *et al.* 2010). We still do not know, however, the cause for the energy difference between upward- and downward-energy EDJs. Finally, we find that EDJs contribute to the  
610 maintenance of the EICs, suggesting that the nonlinear transfer of energy in the statistically steady state is more complex than has been described previously.

A puzzling aspect of our study is that the DEC in Solution 2, with more realistic coastlines and wind forcing, is less realistic than in Solution 1. Intermediate solutions 1.5 and 1.8 show that the  
615 primary factor is the reduction in basin width when coastlines are added. This reduces the speeds and instability of the upper ocean currents, weakening the DEIV, hence leading to a weaker DEC.

## 6.2 *What can we conclude concerning the modeling of DEC?*

620 The DEC is the end result of a series of complex dynamical processes, some being nonlinear in nature: The mean upper-ocean circulation and deep western boundary currents near the equator give rise to instabilities that generate intraseasonal variability; some of that intraseasonal variability propagates away from its source as equatorial waves which then rectify into the mean and slowly varying DEC (Fig. 4). Hence, for a model to reproduce a realistic DEC, it needs to handle correctly  
625 each of these steps, any of which can be impaired by the model's deficiencies, such as a lack of spatial resolution, inadequate forcing, or unrealistic parameterization of subgrid-scale processes.

For the present solutions, the degree of realism of the DEC appears to depend critically on the amplitude and structure of the DEIV. Hence, we speculate that the model's limitations affect (1) the transfer of energy from the upper ocean to the DEIV and/or (2) the transfer of energy from the DEIV to the DEC.

Unfortunately, observations of the DEIV are inadequate for evaluating the DEIV in simulations. As concluded in section 4.1, it is not clear which of our two solutions reproduces the more realistic DEIV. Although the DEIV in Solution 1 may be too energetic over the depth range where it is the strongest (upper 300 m; Fig. 8), it may be more realistic than in Solution 2 at intermediate depths, where the rectification into the DEC is most evident (Fig. 10). Indeed, there is one reason to believe that the deeper DEIV in Solution 1 may be more realistic than in Solution 2: von Schuckmann *et al.* (2008) noticed that the modeled DEIV energy can increase by a factor of 2 to 3 when using a daily rather than a climatological wind forcing. Hence, the unrealistically strong upper-ocean circulation and instabilities of Solution 1 might compensate for the absence of intraseasonal and higher frequency wind forcing and produce a more realistic deeper energy level for the DEIV compared to Solution 2. Together with more observations of the DEIV, an additional simulation similar to Solution 2 but with daily wind forcing would test this interpretation.

Alternatively, the DEIV might be closer to reality in Solution 2 than in Solution 1. In this case, the superior DEC representation in Solution 1 might result from a cancellation of errors: perhaps deficiencies in the model's physics weaken the energy transfer from the DEIV to the DEC, and this is compensated by forcing an unrealistically strong DEIV. Indeed, there are three points supporting this interpretation. First, we know that in a model of a wide basin such as the Pacific, DEIV momentum

dissipation is essential for the EICs to extend westward from their origin (Ascani *et al.* 2010), suggesting that it has to be well parameterized for EICs to have a realistic zonal extent. Second, the DEC is weak or non-existent when horizontal Laplacian friction/diffusion and/or half the horizontal resolution ( $0.5^\circ$  resolution) is used (not shown), suggesting again that the modeled DEC is sensitive to  
655 choices in spatial resolution and subgrid-scale parameterizations. Third, OGCMs have consistently under-estimated the DEC, even when driven with current best estimates of the wind field, and when performing quite well in simulating the upper ocean circulation (Ascani 2005). Additional simulations to study the sensitivity of the energy transfer from DEIV to DEC to a model's resolution and parameters would be needed to confirm this interpretation.

660

### *6.3 Effect of bottom friction*

During the course of performing these experiments, we found that a quadratic bottom drag with a non-dimensional drag coefficient about half the typical value ( $1.225 \times 10^{-3}$  versus  $2.5 \times 10^{-3}$ ) damps  
665 dramatically both the DEIV and the DEC (not shown). This is again consistent with the conclusion that DEIV is the source for the DEC in the simulations and it may explain in part why the DEC is absent in some existing OGCMs. This hypothesis, however, is at odds with previous studies showing that a moderately strong bottom friction is needed to reproduce a realistic level of EKE in OGCMs (Arbic *et al.* 2009).

670

### *6.4 Additional issues*

Other issues have not been addressed in the present study. First, bottom topography is not



included in any of our simulations; given that even simple parameterized bottom friction was found to  
675 reduce DEIV and DEC and was therefore omitted, we expect the roughness and blocking effects of the  
Mid-Atlantic Ridge must be important for the DEIV and the DEC. Second, it is unclear whether the  
zonal jets found poleward of the EICs (*e.g.* Qiu *et al.* 2013) are dynamically similar to the EICs.  
Finally, we have not studied the Lagrangian transport associated with the time-varying DEC, which  
affects the zonal distribution of biogeochemical properties (Getzlaff and Dietze 2013; Dietze and  
680 Lopetien 2013). This transport is a function of the model dissipation (Ascani *et al.* 2010) and the  
analysis of the Lagrangian component of the DEC as a function of subgrid-scale parameterization, in a  
model capable of simulating a realistic DEC, would be needed to address this important issue.

## Acknowledgements

We dedicate this paper to the memory of Bach Lien Hua, who contributed so much to the understanding of the dynamics of the EDJs and EICs. We thank Dailin Wang who actively contributed to the first phase of this study and to Christine Provost and Lucia Bunge who kindly shared their velocity data with us. We also thank the two anonymous reviewers for their constructive comments. The surface drifter climatology of ocean currents has been developed by NOAA/AOML/PMEL and can be found at [http://www.aoml.noaa.gov/phod/dac/dac\\_meanvel.php](http://www.aoml.noaa.gov/phod/dac/dac_meanvel.php). The YoMaHa product is developed by the International Pacific Research Center (IPRC) at the University of Hawaii and is available at <http://apdrc.soest.hawaii.edu/projects/Argo/index.php>. This work was funded in part by NSF Grant OCE0327334 (FA and EF), the IPRC (FA), the German Science Foundation as part of the Sonderforschungsbereich 754 “Climate-Biogeochemistry Interactions in the Tropical Ocean” and by the German Federal Ministry of Education and Research Grant 03F0651B (PB and RJG). PB and RJG are also grateful for continuing support from GEOMAR. Moored velocity observations at the equator were acquired in cooperation with the Prediction and Research Moored Array in the Tropical Atlantic (PIRATA) project. IPRC contribution ##### and SOEST contribution #####.

## References

- Arbic, B. K., J. F. Shriver, P. J. Hogan, H. E. Hurlburt, J. L. McClean, E. J. Metzger, R. B. Scott, A. Sen, O. M. Smedstad, and A. J. Wallcraft, 2009: Estimates of bottom flows and bottom boundary layer dissipation of the oceanic general circulation from global high-resolution models. *J. Geophys. Res.*, **114**, doi:10.1029/2008JC005072
- 705
- Ascani, F., 2005: The equatorial subthermocline circulation in ocean general circulation models. M.S. Thesis, University of Hawaii at Manoa, 67 pp.
- 710 Ascani, F., E. Firing, P. Dutrieux, J. P. McCreary, and A. Ishida, 2010: Deep equatorial ocean circulation induced by a forced-dissipated Yanai beam. *J. Phys. Oceanogr.*, **40**, 1118–1142, doi:10.1175/2010JPO4356.1
- 715 Bourlès, B., M. d'Orgeville, G. Eldin, Y. Gouriou, R. Chuchla, Y. du Penhoat, and S. Arnault, 2002: On the evolution of the thermocline and subthermocline eastward currents in the Equatorial Atlantic. *Geophys. Res. Lett.*, **29**, doi:10.1029/2002GL015098
- Bourlès, B., and Coauthors, 2003: The deep currents in the eastern equatorial Atlantic Ocean. *Geophys. Res. Lett.*, **30**, doi:10.1029/2002GL015095
- 720
- Brandt, P., V. Hormann, B. Bourlès, J. Fischer, F. A. Schott, L. Stramma, and M. Dengler, 2008: Oxygen tongues and zonal currents in the equatorial Atlantic. *J. Geophys. Res.*, **113**, doi:10.1029/2007JC004435
- 725 Brandt, P., A. Funk, V. Hormann, M. Dengler, R. J. Greatbatch, and J. M. Toole, 2011: Interannual atmospheric variability forced by the deep equatorial Atlantic Ocean. *Nature*, **473**, 497501, doi:10.1038/nature10013
- Brandt, P., and Coauthors, 2012: Ventilation of the equatorial Atlantic by the equatorial deep jets. *J.*

Bunge, L., C. Provost, B. L. Hua, and A. Kartavtseff, 2008: Variability at intermediate depths at the equator in the Atlantic Ocean in 2000-06: Annual cycle, equatorial deep jets, and intraseasonal meridional velocity fluctuations. *J. Phys. Oceanogr.*, **38**, 1794–1806, doi:10.1175/2008JPO3781.1

735

Cane, M. A., and D. W. Moore, 1981: A note on low-frequency equatorial basin modes. *J. Phys. Oceanogr.*, **11**, 1578–1584, doi:10.1175/1520-0485(1981)011<1578:ANOLFE>2.0.CO;2

740

Cravatte, S., W. S. Kessler, and F. Marin, 2012: Intermediate zonal jets in the tropical Pacific Ocean observed by Argo floats. *J. Phys. Oceanogr.*, **42**, 1475–1485, doi:10.1175/JPO-D-11-0206.1

Czeschel, R., L. Stramma, F. U. Schwarzkopf, B. S. Giese, A. Funk, and J. Karstensen, 2011: Middepth circulation of the eastern tropical South Pacific and its link to the oxygen minimum zone. *J. Geophys. Res.*, **116**, doi:10.1029/2010JC006565

745

Dietze, H., and U. Loeptien, 2013: Revisiting “nutrient trapping” in global coupled biogeochemical ocean circulation models. *Global Biogeochem. Cycles*, **7**, 265–284, doi:10.1002/gbc.20029

750

d'Orgeville, M., B. L. Hua, and H. Sasaki, 2007: Equatorial Deep Jets triggered by a large vertical scale variability within the western boundary layer. *J. Mar. Res.*, **65**, 1–25, doi:10.1357/002224007780388720

Eden, C., 2006: Middepth equatorial tracer tongues in a model of the Atlantic Ocean. *J. Geophys. Res.*, **111**, doi:10.1029/2006JC003565

755

Eden, C., and M. Dengler, 2008: Stacked jets in the deep equatorial Atlantic Ocean. *J. Geophys. Res.*, **113**, doi:10.1029/2007JC004298

Firing, E., 1987: Deep zonal currents in the central equatorial Pacific. *J. Mar. Res.*, **45**, 791–812,

Firing, E., S. Wijffels, and P. Hacker, 1998: Equatorial subthermocline currents across the Pacific. *J. Geophys. Res.*, **103**, 21413–21423, doi:10.1029/98JC01944

765      Getzlaff, J., and H. Dietze, 2013: Effects of increased isopycnal diffusivity mimicking the unresolved equatorial intermediate current system in an earth system climate model. *Geophys. Res. Lett.*, **40**, 2166–2170, doi:10.1002/grl.50419

770      Gill, A. E., 1974: The stability of planetary waves on an infinite beta-plane. *Geophys. Astrophys. Fluid Dyn.*, **6**, 29–47, doi:10.1080/03091927409365786

Gill, A. E., 1982: *Atmosphere-ocean dynamics*. Academic Press, 662 pp.

775      Gouriou, Y., B. Boulès, H. Mercier, and R. Chuchla, 1999: Deep jets in the equatorial Atlantic Ocean. *J. Geophys. Res.*, **104**, 21217–21226, doi:10.1029/1999JC900057

Gouriou, Y., and Coauthors, 2001: Deep circulation in the equatorial Atlantic Ocean. *Geophys. Res. Lett.*, **28**, 819–822, doi:10.1029/2000GL012326

780      Greatbatch, R. J., P. Brandt, M. Claus, S.-H. Didwischus, and Y. Fu, 2012: On the width of the equatorial deep jets. *J. Phys. Oceanogr.*, **42**, 17291740, doi:10.1175/JPO-D-11-0238.1

Hayashi, Y., 1982: Interpretations of space-time spectral energy equations. *J. Atmos. Sci.*, **39**, 685–688, doi:10.1175/1520-0469(1982)039<0685:IOSTSE>2.0.CO;2

785

Hua, B. L., M. d'Orgeville, M. D. Fruman, C. Ménesguen, R. Schopp, P. Klein, and H. Sasaki, 2008: Destabilization of mixed Rossby gravity waves and the formation of equatorial zonal jets. *J. Fluid Mech.*, **610**, 311–341, doi:10.1017/S0022112008002656

- 790 Ishida, A., Y. Kashino, H. Mitsudera, N. Yosioka, and T. Kadokura, 1998: Preliminary results of a  
global high-resolution GCM experiment. *J. Fac. Sci. Hokkaido Univ.*, **11**, 441–460.
- Johnson, G. C., E. Kunze, K. E. McTaggart, and D. W. Moore, 2002: Temporal and spatial structure of  
the equatorial deep jets in the Pacific Ocean. *J. Phys. Oceanogr.*, **32**, 3396–3407,  
795 doi:10.1175/1520-0485(2002)032<3396:TASSOT>2.0.CO;2
- Johnson, G. C., and D. Zhang, 2003: Structure of the Atlantic Ocean equatorial deep jets. *J. Phys.  
Oceanogr.*, **33**, 600–609, doi:10.1175/1520-0485(2003)033<0600:SOTAOE>2.0.CO;2
- 800 Kessler, W. S., G. C. Johnson, and D. W. Moore, 2003: Sverdrup and nonlinear dynamics of the Pacific  
Equatorial currents. *J. Phys. Oceanogr.*, **33**, 994–1008, doi:dx.doi.org/10.1175/1520-  
0485(2003)033<0994:SANDOT>2.0.CO;2
- Lebedev, K. V., H. Yoshinari, N. A. Maximenko, P. W. Hacker, 2007: YoMaHa’07: Velocity data  
805 assessed from trajectories of Argo floats at parking level and at the sea surface. *IPRC Tech. Note 4*,  
16 pp.
- Lumpkin, R., and S. L. Garzoli, 2005: Near-surface circulation in the Tropical Atlantic Ocean. *Deep-  
Sea Res. I*, **52**, 495–518, doi:10.1016/j.dsr.2004.09.001
- 810
- Luyten, J. R., and F. C. Swallow, 1976: Equatorial undercurrents. *Deep-Sea Res.*, **23**, 999–1001,  
doi:10.1016/0011-7471(76)90830-5
- Maltrud, M. E., and J. L. McClean, 2005: An eddy resolving global  $1/10^\circ$  ocean simulation. *Ocean*  
815 *Modell.*, **8**, 31–54, doi:10.1016/j.ocemod.2003.12.001
- McPhaden, M. J., and P. Ripa, 1990: Wave-mean flow interactions in the equatorial ocean. *Annu. Rev.  
Fluid Mech.*, **22**, 167–205, doi:10.1146/annurev.fl.22.010190.001123

- 820 Ménesguen, C., B. L. Hua, M. D. Fruman, and R. Schopp, 2009: Dynamics of the combined Extra-Equatorial and Equatorial Deep jets in the Atlantic. *J. Mar. Res.*, **67**, 323–346, doi:10.1357/002224009789954766
- Ollitrault, M., M. Lankhorst, D. Fratantoni, P. Richardson, and W. Zenk, 2006: Zonal intermediate  
825 currents in the equatorial Atlantic Ocean. *Geophys. Res. Lett.*, **33**, doi:10.1029/2005GL025368
- Ollitrault, M., and A. Colin de Verdière, 2014: The ocean general circulation near 1000-m depth. *J. Phys. Oceanogr.*, **44**, 384–409, doi:10.1175/JPO-D-13-030.1
- 830 Pacanowski, R., and S. Philander, 1981: Parametrization of vertical mixing in numerical models of tropical oceans. *J. Phys. Oceanogr.*, **11**, 1443–1451, doi:10.1175/1520-0485(1981)0112.0.CO;2
- Pedlosky, J., 1996: *Ocean circulation theory*. Springer-Verlag, 453 pp.
- 835 Proehl, J. A., 1990: Equatorial wave-mean flow interaction: The long Rossby waves. *J. Phys. Oceanogr.*, **20**, 274–294, doi:10.1175/1520-0485(1990)020<0274:EWMFIT>2.0.CO;2
- Qiu, B., S. Chen, and H. Sasaki, 2013: Generation of the North Equatorial Undercurrent jets by triad baroclinic Rossby wave interactions. *J. Phys. Oceanogr.*, **43**, 2682–2698, doi:10.1175/JPO-D-13-  
840 099.1
- Saltzman, B., 1957: Equations governing the energetics of the larger scales of atmospheric turbulent in the domain of wave number. *J. Meteor.*, **14**, 513–523, doi:10.1175/1520-0469(1957)014<0513:EGTEOT>2.0.CO;2
- 845 Schott, F. A., L. Stramma, and J. Fischer, 1995: The warm water inflow into the western tropical Atlantic boundary regime, spring 1994. *J. Geophys. Res.*, **100**, 24745–24760, doi:10.1029/95JC02803

- 850 Schott, F. A., J. Fischer, and L. Stramma, 1998: Transports and pathways of the upper-layer circulation  
in the western tropical Atlantic. *J. Phys. Oceanogr.*, **28**, 1904–1928,  
doi:10.1175/1520-0485(1998)028<1904:TAPOTU>2.0.CO;2
- Schott, F. A., and Coauthors, 2003: The zonal currents and transports at 35°W in the tropical Atlantic.  
855 *Geophys. Res. Lett.*, **30**, 1349–1352, doi:10.1029/2002GL016849
- Send, U., C. Eden, and F. Schott, 2002: Atlantic equatorial deep jets: Space-time structure and cross-  
equatorial fluxes. *J. Phys. Oceanogr.*, **32**, 891–902, doi:10.1175/1520-  
0485(2002)032<0891:AEDJST>2.0.CO;2
- 860
- Stommel, H. M., 1982: Is the South Pacific helium-3 plume dynamically active? *Earth Planet. Sci.*  
*Lett.*, **61**, 63–67, doi:10.1016/0012-821X(82)90038-3
- Stramma, L., S. Hüttl, and J. Schafstall, 2005: Water masses and currents in the upper tropical  
865 northeast Atlantic off northwest Africa. *J. Geophys. Res.*, **110**, doi:10.1029/2005JC002939
- Stramma, L., G. C. Johnson, E. Firing, and S. Schmidtke, 2010: Eastern Pacific oxygen minimum  
zones: Supply paths and multidecadal changes. *J. Geophys. Res.*, **115**, doi:10.1029/2009JC005976
- 870 Thierry, V., A.-M. Treguier, and H. Mercier, 2004: Numerical study of the annual and semi-annual  
fluctuations in the deep equatorial Atlantic Ocean. *Ocean Modell.*, **6**, 1–30,  
doi:10.1016/S1463-5003(02)00054-9
- von Schuckmann, K., P. Brandt, and C. Eden, 2008: Generation of tropical instability waves in the  
875 Atlantic Ocean. *J. Geophys. Res.*, **113**, doi:10.1029/2007JC004712
- Youngs, M. K., and G. C. Johnson, 2015: Basin-wavelength Equatorial Deep Jet signal across three  
oceans. Submitted to *J. Phys. Oceanogr.*



# Table Caption List

**Table 1:** List of abbreviations for currents and ocean motions used in the text.

885 **Table 2:** General characteristics of the configuration of each numerical solution. In each case, the wind stress is derived from observed winds over the Atlantic Ocean from the European Remote Sensing (ERS-1/2) scatterometer product. The realism of the configuration increases from top to bottom.

## Tables

| Abbreviation | Meaning                                   |
|--------------|---|
| DEC          | deep equatorial circulation               |
| DWBC         | deep western boundary current             |
| DEIV         | deep equatorial intraseasonal variability |
| EDJs         | Equatorial Deep Jets                      |
| EICs         | Equatorial Intermediate Currents          |
| LEIC         | Lower Equatorial Intermediate Current     |
| MRG          | mixed Rossby-gravity                      |
| NBC          | North Brazil Current                      |
| NECC         | North Equatorial Countercurrent           |
| NEIC         | North Equatorial Intermediate Current     |
| NICC         | North Intermediate Countercurrent         |
| SEC          | South Equatorial Current                  |
| SEIC         | South Equatorial Intermediate Current     |
| SICC         | South Intermediate Countercurrent         |
| TIWs         | Tropical Instability Waves                |

**Table 1:** List of abbreviations for currents and ocean motions used in the text.

| Name         | Coastline   | Wind Stress  |
|--------------|-------------|--|
| Solution 1   | rectangular | time and zonally independent with a realistic meridional profile |
| Solution 1.5 | realistic   | time and zonally independent with a realistic meridional profile |
| Solution 1.8 | realistic   | time independent with a realistic zonal and meridional profile   |
| Solution 2   | realistic   | varies climatologically, zonally and meridionally                |

**Table 2:** General characteristics of the configuration of each numerical solution. In each case, the wind stress is derived from observed winds over the Atlantic Ocean from the European Remote Sensing (ERS-1/2) scatterometer product. The realism of the configuration increases from top to bottom.

## Figure Caption List

**Figure 1:** (a) Mean zonal component of velocity ( $u$ ) at  $159^\circ\text{W}$  (from 21 cruises between March 1982 and June 1983; see Firing 1987). (b) Mean  $u$  at  $35^\circ\text{W}$  (from 10 cruises between 1990 and 2003; see Eden and Dengler 2008). (c) A quasi-synoptic section of  $u$  from the data along  $159^\circ\text{W}$  (May-June 1982). (d) A quasi-synoptic section of  $u$  from the data along  $35^\circ\text{W}$  (May 2003). EICs: Equatorial Intermediate Currents; EDJs: Equatorial Deep Jets. Notice the different color scale for the quasi-synoptic sections and the means. The EDJs do not appear in (b) because the time span of measurements used for the average ( $\sim 13$  years) is 2 to 3 times longer than the period of the EDJs ( $5 \pm 1$  years; Johnson and Zhang 2003).

**Figure 2:** Time series of equatorial  $u$  at  $23^\circ\text{W}$  in (a) the observations of Brandt *et al.* (2011), (b) Solution 1, and (c) Solution 2.

**Figure 3:** (a) Mean (1997-2014)  $u$  at 1000 m from the net displacements of Argo floats at their parking depth, using the YoMaHa product (Lebedev *et al.* 2007; Ascani *et al.* 2010). (b) Mean eddy kinetic energy (EKE) from the  $v$  component only (that is,  $1/2 \langle (v - \langle v \rangle)^2 \rangle$  where the angle brackets indicate the 1997-2014 mean) from the same dataset. The quantities have been calculated over a  $1^\circ \times 1^\circ$  grid. There are about 10 samples per bin on average and white bins have no observations. Blue frames in (b) indicate regions of DEIV.

**Figure 4:** Two scenarios proposed for the generation of the deep equatorial circulation (DEC) in the Atlantic Ocean. Both involve the rectification of deep equatorial intraseasonal variability (DEIV). In scenario (a), proposed by d'Orgeville *et al.* (2007) and Ménesguen *et al.* (2009) and built on the work of Hua *et al.* (2008), DEIV is generated directly at depth by the instability of the deep western boundary current (DWBC) crossing the equator. In scenario (b), proposed by Ascani *et al.* (2010), DEIV is generated away from the western boundary by the instability of the wind-driven upper-ocean circulation, such as Tropical Instability Waves (TIWs). The red arrows indicate the main direction of DEIV energy propagation in each scenario.

**Figure 5:** 5-year mean near-surface  $u$  (left) and EKE (right) in (upper) the observations, (middle) Solution 1 and (lower) Solution 2. Observations are from the Global Drifter Program ([http://www.aoml.noaa.gov/phod/dac/dac\\_meanvel.php](http://www.aoml.noaa.gov/phod/dac/dac_meanvel.php); Lumpkin and Johnson, 2013). The velocity anomaly from the mean and seasonal cycle are used to construct EKE in both the observations and the simulations. Years 25 to 29 are used for the two runs. The black line corresponds to the coastline in the upper panels and to the 200-m isobath in the lower panels.

**Figure 6:** Time series of the meridional component of velocity,  $v$ , at (a) ( $23^\circ\text{W}$ ,  $5^\circ\text{N}$ ) and (b) ( $23^\circ\text{W}$ ,  $0^\circ\text{N}$ ) in Solution 1. Frequency-horizontal wavenumber ( $\omega-k$ ) spectrum of  $v$  along (c)  $5^\circ\text{N}$  and (d)  $0^\circ\text{N}$ . Frequency-vertical mode number ( $\omega-n$ ) spectrum of  $v$  along (e)  $5^\circ\text{N}$  and (f)  $0^\circ\text{N}$ . Years 25 to 34 are used to construct all spectra. The  $\omega-k$  spectrum in (c) is the average of spectra computed at every level below 1000 m depth while the  $\omega-k$  spectrum in (d) is the spectrum for the 12<sup>th</sup> baroclinic mode only. The  $\omega-n$  spectrum is the average of spectra computed every  $2^\circ$  in longitude. All spectra are normalized by their maximum value before being plotted on a logarithmic scale. The black curves in (c) show the dispersion relations for the Rossby waves with  $n=0$  and zero-meridional wavenumber ( $l=0$ ), and with  $n=2$  and  $l=1/10^\circ$  cycles-per-degree. The black curve in (d) shows the dispersion relation for the  $n=12$  MRG wave while the black curve in (f) shows the dispersion relation for all baroclinic MRG waves with a  $8^\circ$  zonal wavelength.

**Figure 7:** Power density spectrum of equatorial  $v$  zonally and vertically averaged in Solutions 1 and 2. One-year-long time series from every  $5^\circ$  in longitude and 500 m in the vertical (between 1000 and 5000 m) are considered independent and used to compute the averaged spectrum. Each is detrended and a Hanning window is applied to it before performing the Fourier decomposition. This results in 630 segments with 1680 degrees of freedom (*dof*) in both cases (years 24 to 28). The same qualitative result is obtained if we use  $35^\circ\text{W}$  instead of  $23^\circ\text{W}$  for Solution 1;  $35^\circ\text{W}$  is the same distance from the western boundary at the equator in Solution 1 as  $23^\circ\text{W}$  is in the ocean (Fig. 5). The 95% confidence intervals are shown with vertical bars and are computed as described in von Storch and Zwiers (1999).

**Figure 8:** Variance-preserving power density spectra of equatorial  $v$  at  $23^\circ\text{W}$  in (a) observations, (b) Solution 1 and (c) Solution 2. Spectral calculations are identical to those of Fig. 7 except that they are performed at every available depth and only at  $23^\circ\text{W}$ . This results in 5.4 segments on average for each depth (*dof*=14) for the observations, 8 segments per depth (*dof*=21; years 24 to 31) for Solution 1 and

6 segments per depth ( $dof=16$ ; years 24 to 30) for Solution 2. The observations are those reported in Brandt *et al.* (2012; 10-year long coverage).

**Figure 9:** Model-data comparisons of power density spectrum of equatorial  $v$ : (blue) observations, (red) Solution 1 and (green) Solution 2. Spectral calculations are conducted as for the spectra of Fig. 7 except that to construct the model spectra, we use only locations that are near the actual locations of the moorings and either one-year or 20-month long segments depending on the duration of the data: (a) observations at 23°W described in Bunge *et al.* (2008), a total of 9 one-year long segments ( $dof=32$ ) from 7 depths between 635 and 1486 m depth; (b) observations at 10°W also described in Bunge *et al.* (2008), a total of 15 one-year long segments ( $dof=40$ ) from 9 depths between 764 and 1689 m depth; (c) observations from the ACM10 mooring, a total of 3 20-month long segments ( $dof=8$ ) at 3, 3.6 and 4.1 km depth; and (d) observations from the ACM11 mooring, a total of 3 one-year long segments ( $dof=8$ ) at 1.7, 2 and 2.8 km depth. The longitude and depth range of each dataset is shown in the inlet panel in (a). Vertical dashed lines delimits the intraseasonal waveband (15-to-60-day period).

**Figure 10:** Mean EKE near 1000 m depth from the  $v$  component only (that is,  $1/2 \langle (v - \langle v \rangle)^2 \rangle$  where the angle brackets indicate the time average): (a) from Argo data as in Fig. 3 (panel b), (b) in Solution 1 and (c) in Solution 2. Average is over 1997-2014 for (a), and years 25 to 29 for (b) and (c). The model data have been low-pass filtered using a 10-day running mean before calculating the mean EKE in order to mimic the typical sampling scheme of the Argo data (about once every 10 days).

**Figure 11:** (left) 5-day mean, (middle) 6-month and (right) 5-year mean  $u$  at 34°W in (upper) Solution 1 and (lower) Solution 2. For both runs, the 5-day mean on June 1 of year 29, the second half of year 29 and years 25 to 29 are used for the 5-day average, the 6-month mean and the 5-year mean, respectively. Notice the different color scale for the 5-day averages and for the 6-month and 5-year means.

**Figure 12:** Mean  $u$  at 1000 m (upper) from Argo float displacements (see caption of Fig. 3) (middle) in Solution 1 and (lower) in Solution 2. Years 25 to 29 are used for Solution 1 and 2.

**Figure 13:** (upper) Time series of equatorial low-frequency (period > 1.75 year)  $u$  at 23°W in Solution 1. Velocity profiles below 300 m have been vertically stretched and scaled (using a reference buoyancy frequency of 1 cph; Gill 1982) before being plotted; the stretched and unstretched depth ticks are

shown on the left and right axes, respectively. In the middle and lower panels are plotted the squared amplitude averaged along the equator of the downward and upward energy propagating  $u$ , respectively. The anomalously high values near 3100 stretched meters depth in these two panels result from unrealistically weak stratification in the reference profile at this depth.

**Figure 14:** Spectrum of equatorial  $u$  in the frequency-vertical wavenumber space: (a) Solution 1 (years 10 to 49) and (b) Solution 2 (years 24 to 29). Each spectrum is the average of spectra calculated every  $2^\circ$  along the equator and is normalized by its maximum value before being plotted on a logarithmic scale. For Solution 1, the spectrum is computed from a set of 15-year time series shifted in time every 2.5 years; for Solution 2, the full time series between years 24 and 29 is used. Velocity profiles below 300 m are stretched and scaled as in Fig. 13 before computing the spectra. The dotted black lines show the distribution of energy expected for low-frequency baroclinic equatorial basin modes (Eq. (1); Cane and Moore 1981).

**Figure 15:** Meridional and temporal structure of upward-energy  $u$  at the 3.9-year period and 930 stretched meters vertical wavelength (vertical mode 12): (upper) from Solution 1 and (lower) from the theory of Cane and Moore (1981), with a Rayleigh damping coefficient  $r = r_0 \cdot [1, 2, \dots, l]$  that is linearly increasing with the absolute meridional mode number  $|l|$  with  $r_0 = 2 \times 10^{-9} \text{ s}^{-1}$ . The longitudes are (left)  $40^\circ\text{W}$ , (middle)  $20^\circ\text{W}$  and (right)  $0^\circ\text{E}$ . The abscissa is phase in radians over one period. The model and analytical solution have each been normalized by the maximum of its absolute value over the whole domain.

**Figure 16:** Zonal kinetic energy budget: Contribution to  $\partial_t u^2$  in the frequency-vertical wavenumber space by the real part of (a)  $-\hat{u}^* \cdot (\widehat{v u_y})$ , (b)  $\hat{u}^* \cdot (-\widehat{u u_x} - \widehat{w u_z} - \widehat{p_x} / \rho_0 + \widehat{D_V^x})$ , (c)  $-\hat{u}^* \cdot (\widehat{u u_x})$ , (d)  $-\hat{u}^* \cdot (\widehat{w u_z})$  (e)  $-\hat{u}^* \cdot (\widehat{p_x} / \rho_0)$  and (f)  $\hat{u}^* \cdot \widehat{D_V^x}$  along the equator in Solution 1; see text for details. The term  $\hat{u}^* \cdot \widehat{D_H^x}$  is weak and is not shown. Velocities from years 10 to 49 and below 300 m are stretched and scaled as in Fig. 13 before computing the spectra. The spectra are calculated every  $2^\circ$  in longitude and then averaged. The small box in (a) corresponds to the LEIC that is the focus of Figs. 17, 18 and 19 while the circle marks a basin mode that composes the EDJs and is the focus of Fig. 20. The dotted black lines show the basin mode dispersion relation as in Fig. 14.

**Figure 17:** Nonlinear energy transfer (in frequency-vertical wavenumber space) to the LEIC ( $f_0=0$  and  $m_0=0$ ; square symbol in Fig. 16a) *via* the term  $-vu_y$  in Solution 1, that is quantity (5). Positive (red/yellow) values indicate a transfer of energy to LEIC and the reverse for negative values (blue/cyan).  $(f_i, m_i)$  are the frequency and wavenumber (in stretched vertical coordinate) of the wave  $i=1,2$ . Spectra are calculated as in Fig. 16 but for 20-year long segments with 50% overlap, then averaged.

**Figure 18:** Nonlinear energy transfer (in frequency-vertical wavenumber space) to the LEIC ( $f_0=0$  and  $m_0=0$ ; square symbol in Fig. 16a) *via* the term  $-uu_x$  in Solution 1, that is quantity (6). See caption of Fig. 17 for details.

**Figure 19:** Nonlinear energy transfer (in physical space) from a particular EDJ basin mode to EICs *via* the term  $-uu_x$ , that is quantity (7). The EDJs used in this calculation correspond to the theoretical basin mode shown in the lower panels of Fig. 15 with a maximum amplitude of 10 cm/s, while the EICs are defined as the time and vertical averaged zonal velocity below 300 m from Solution 1 (years 25 to 29). Contours of EICs in cm/s are plotted in black.

**Figure 20:** Nonlinear transfer of energy (in frequency-vertical wavenumber space) to (a) the Kelvin wave component – that is quantity (10) – and (b) long Rossby wave component – that is quantity (11) – of a particular EDJ basin mode ( $f_0=1/5.5$  cycles-per-year and  $m_0=1/645$  cycles-per-meter; circle symbol in Fig. 16a) *via* the nonlinear term  $-vu_y$  in Solution 1. The meaning of the color code is the same as in Fig. 17.  $(f_i, m_i)$  are the frequency and wavenumber (in stretched vertical coordinate) of the wave  $i=1,2$ . Spectra are calculated as in Fig. 16 but for 5.5-year long segments with 50% overlap then averaged.



## Figures

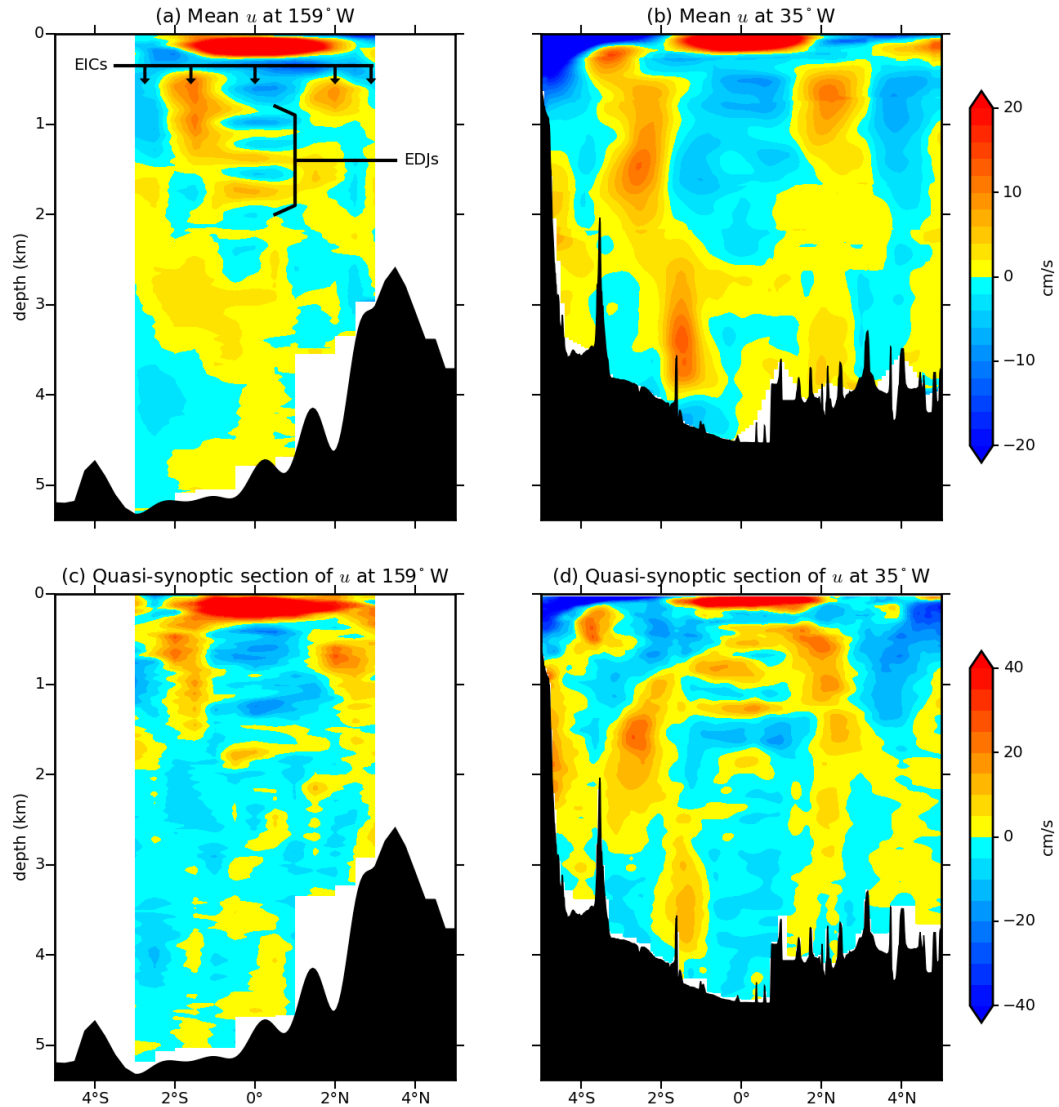


**Figure 1:** (a) Mean zonal component of velocity ( $u$ ) from shipboard observations at 159°W (21 cruises between March 1982 and June 1983; see Firing 1987). (b) Mean  $u$  from shipboard observations at 35°W (10 cruises between 1990 and 2003; see Eden and Dengler 2008). (c) A quasi-synoptic section of  $u$  out of the dataset at 159°W (May-June 1982). (d) A quasi-synoptic section of  $u$  out of the dataset at 35°W (May 2003). EICs: Equatorial Intermediate Currents; EDJs: Equatorial Deep Jets. Notice the different color scale for the quasi-synoptic sections and the means. The EDJs do not appear in (b) because the time span of measurements used for the average ( $\sim 13$  years) is 2 to 3 times longer than the period of the EDJs ( $5 \pm 1$  years; Johnson and Zhang 2003).

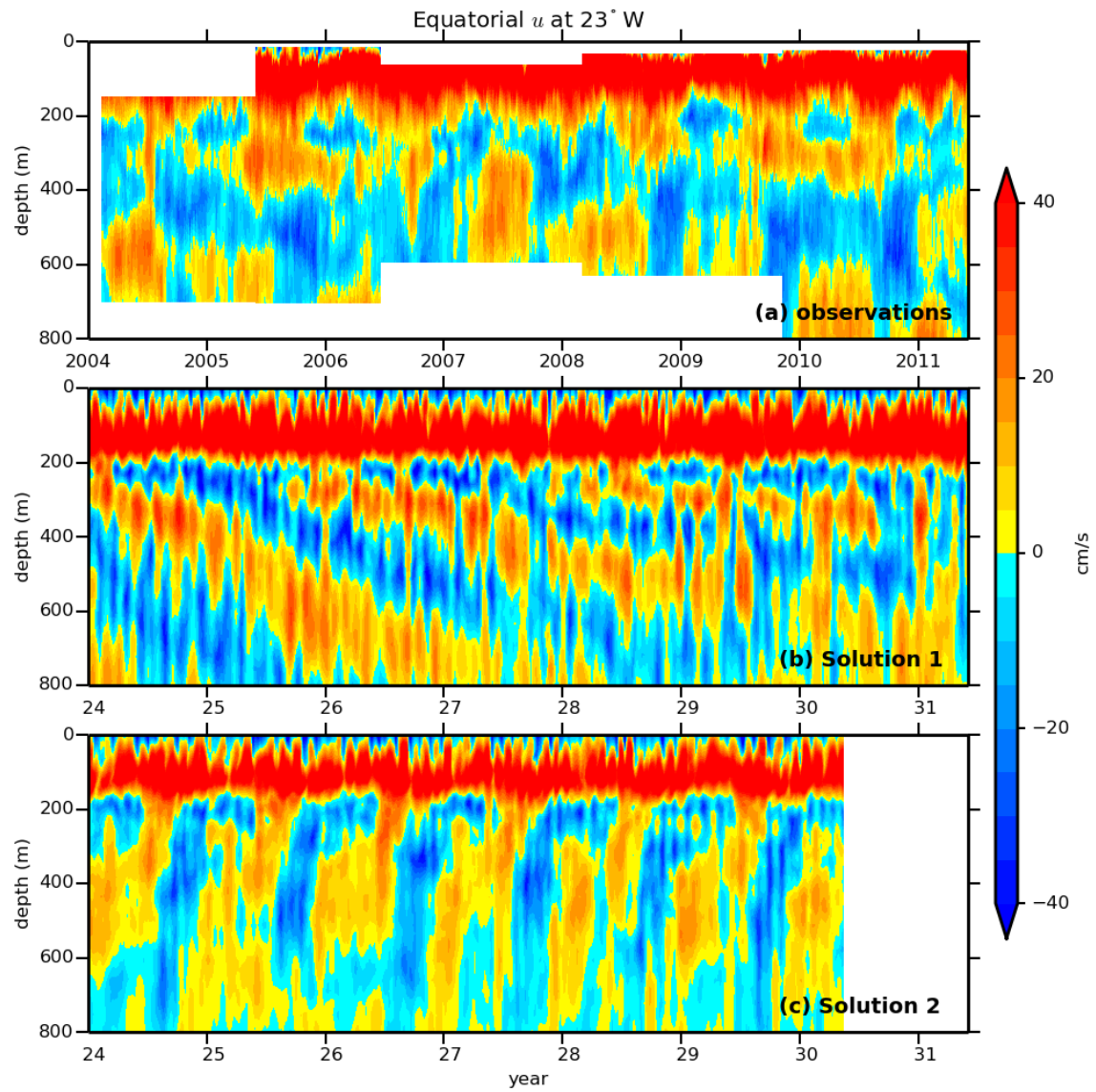


**Figure 2:** Time series of equatorial  $u$  at  $23^\circ$ W in (a) the observations of Brandt *et al.* (2011; 2012), (b) Solution 1, and (c) Solution 2.

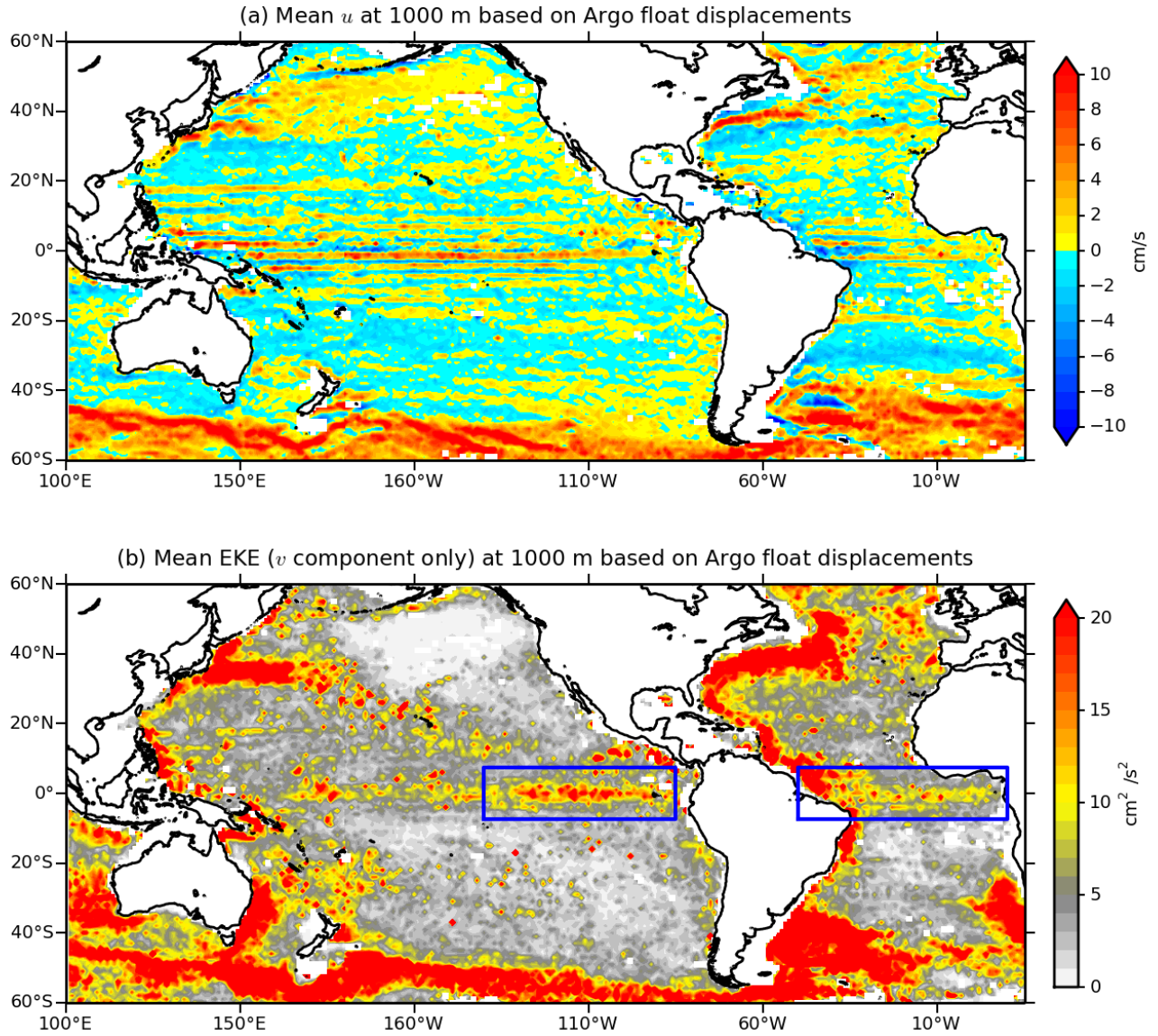


**Figure 3:** (a) Mean (1997-2014)  $u$  at 1000 m from the net displacements of Argo floats at their parking depth, using the YoMaHa product (Lebedev *et al.* 2007; Ascani *et al.* 2010). (b) Mean eddy kinetic energy (EKE) from the  $v$  component only (that is,  $1/2 \langle (v - \langle v \rangle)^2 \rangle$  where the angle brackets indicate the 1997-2014 mean) from the same dataset. The quantities have been calculated over a  $1^\circ \times 1^\circ$  grid. There are about 10 samples per bin on average and white bins have no observations. Blue frames in (b) indicate regions of DEIV.

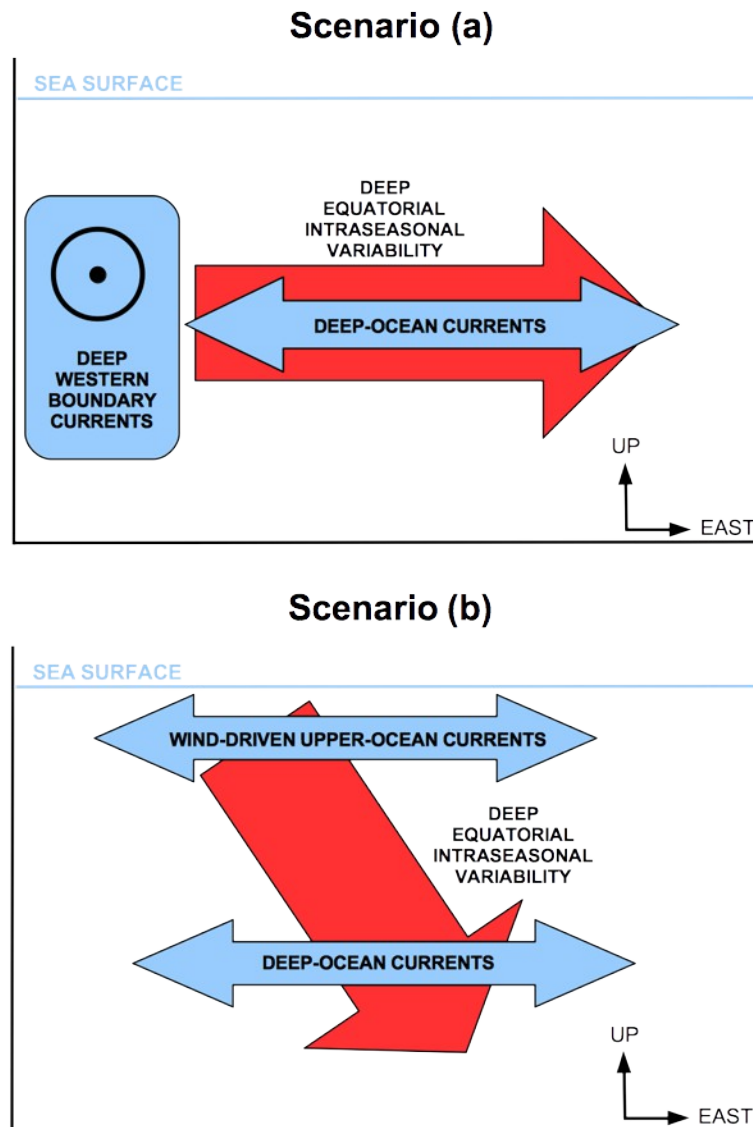


**Figure 4:** Two scenarios proposed for the generation of the deep equatorial circulation (DEC) in the Atlantic Ocean. Both involve the rectification of deep equatorial intraseasonal variability (DEIV). In scenario (a), proposed by d'Orgeville *et al.* (2007) and Ménesguen *et al.* (2009) and built on the work of Hua *et al.* (2008), DEIV is generated directly at depth by the instability of the deep western boundary current (DWBC) crossing the equator. In scenario (b), proposed by Ascani *et al.* (2010), DEIV is generated away from the western boundary by the instability of the wind-driven upper-ocean circulation, such as Tropical Instability Waves (TIWs). The red arrows indicate the main direction of DEIV energy propagation in each scenario.

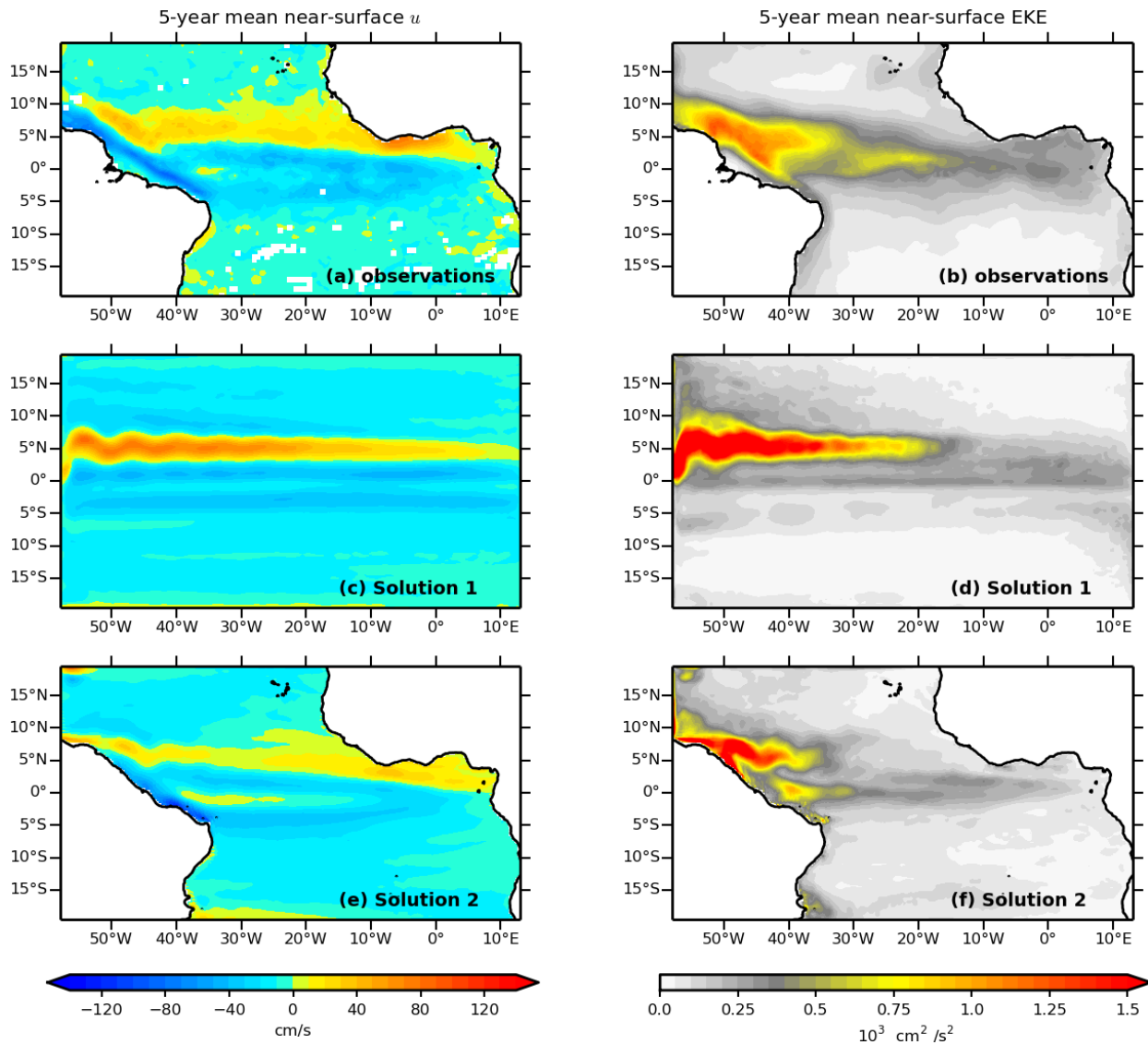


**Figure 5:** 5-year mean near-surface  $u$  (left) and EKE (right) in (upper) the observations, (middle) Solution 1 and (lower) Solution 2. Observations are from the Global Drifter Program ([http://www.aoml.noaa.gov/phod/dac/dac\\_meanvel.php](http://www.aoml.noaa.gov/phod/dac/dac_meanvel.php); Lumpkin and Johnson, 2013). The velocity anomaly from the mean and seasonal cycle are used to construct EKE in both the observations and the simulations. Years 25 to 29 are used for the two runs. The black line corresponds to the coastline in the upper panels and to the 200-m isobath in the lower panels.

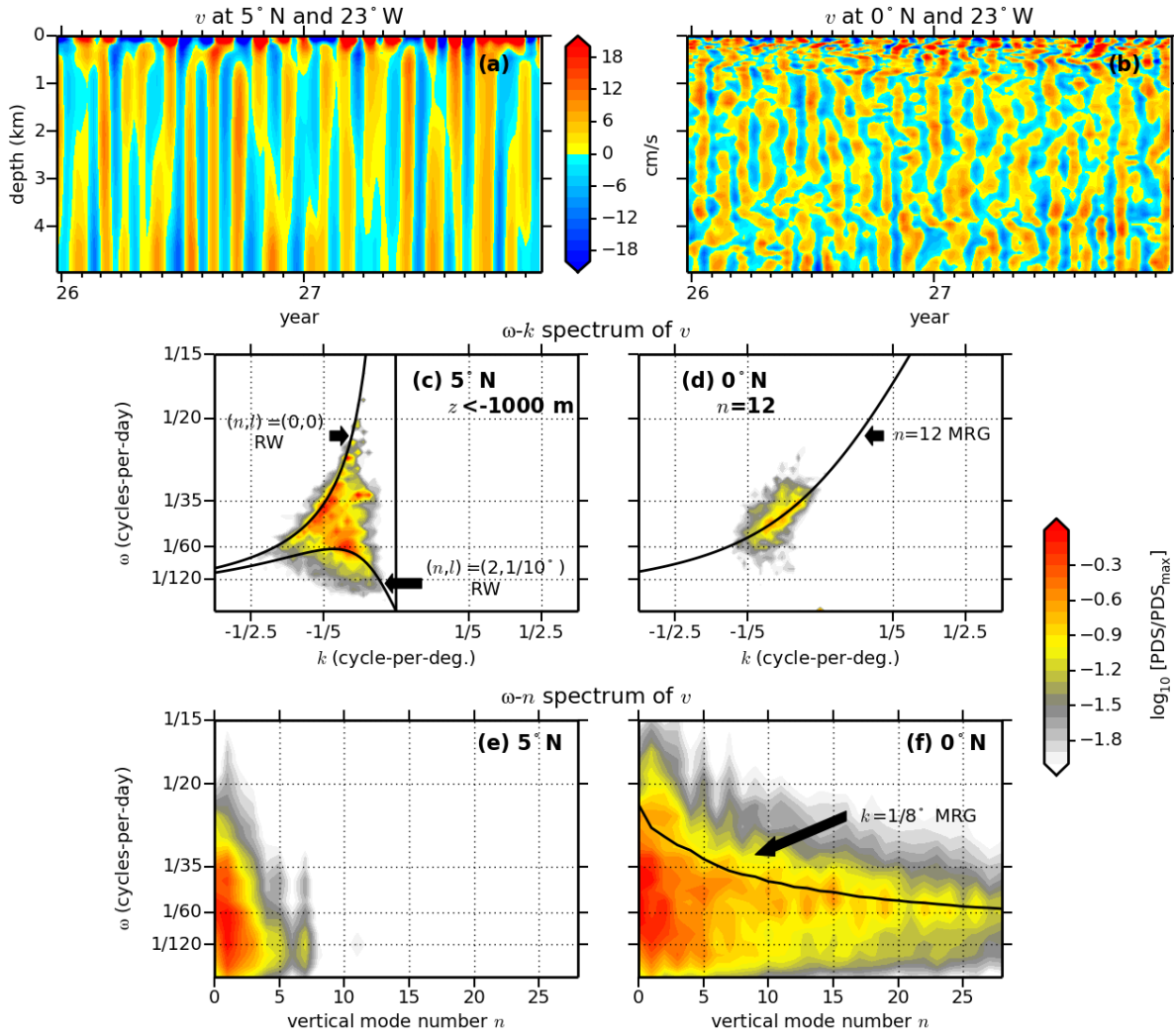


**Figure 6:** Time series of the meridional component of velocity,  $v$ , at (a) ( $23^\circ\text{W}$ ,  $5^\circ\text{N}$ ) and (b) ( $23^\circ\text{W}$ ,  $0^\circ\text{N}$ ) in Solution 1. Frequency-horizontal wavenumber ( $\omega$ - $k$ ) spectrum of  $v$  along (c)  $5^\circ\text{N}$  and (d)  $0^\circ\text{N}$ . Frequency-vertical mode number ( $\omega$ - $n$ ) spectrum of  $v$  along (e)  $5^\circ\text{N}$  and (f)  $0^\circ\text{N}$ . Years 25 to 34 are used to construct all spectra. The  $\omega$ - $k$  spectrum in (c) is the average of spectra computed at every level below  $1000\text{ m}$  depth while the  $\omega$ - $k$  spectrum in (d) is the spectrum for the  $12^{\text{th}}$  baroclinic mode only. The  $\omega$ - $n$  spectrum is the average of spectra computed every  $2^\circ$  in longitude. All spectra are normalized by their maximum value before being plotted on a logarithmic scale. The black curves in (c) show the dispersion relations for the Rossby waves with  $n=0$  and zero-meridional wavenumber ( $l=0$ ), and with  $n=2$  and  $l=1/10^\circ$  cycles-per-degree. The black curve in (d) shows the dispersion relation for the  $n=12$  MRG wave while the black curve in (f) shows the dispersion relation for all baroclinic MRG waves with a  $8^\circ$  zonal wavelength.



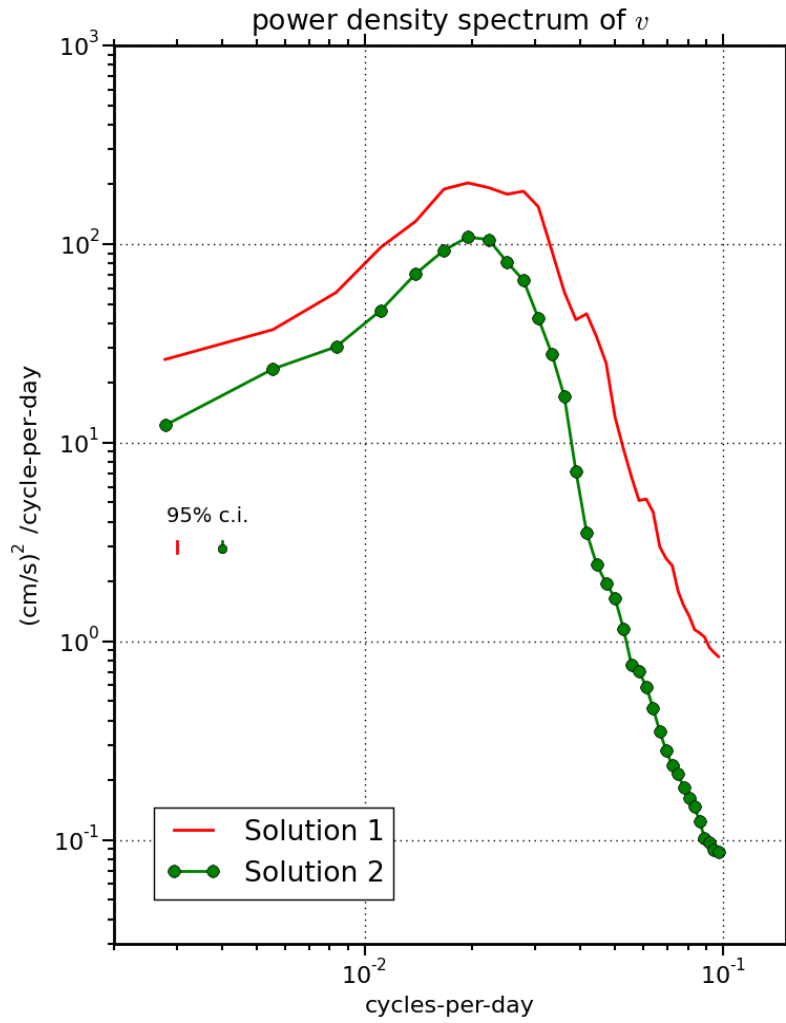


**Figure 7:** Power density spectrum of equatorial  $v$  zonally and vertically averaged in Solutions 1 and 2. One-year-long time series from every  $5^\circ$  in longitude and 500 m in the vertical (between 1000 and 5000 m) are considered independent and used to compute the averaged spectrum. Each is detrended and a Hanning window is applied to it before performing the Fourier decomposition. This results in 630 segments with 1680 degrees of freedom (*dof*) in both cases (years 24 to 28). The same qualitative result is obtained if we use  $35^\circ\text{W}$  instead of  $23^\circ\text{W}$  for Solution 1;  $35^\circ\text{W}$  is the same distance from the western boundary at the equator in Solution 1 as  $23^\circ\text{W}$  is in the ocean (Fig. 5). The 95% confidence intervals are shown with vertical bars and are computed as described in von Storch and Zwiers (1999).



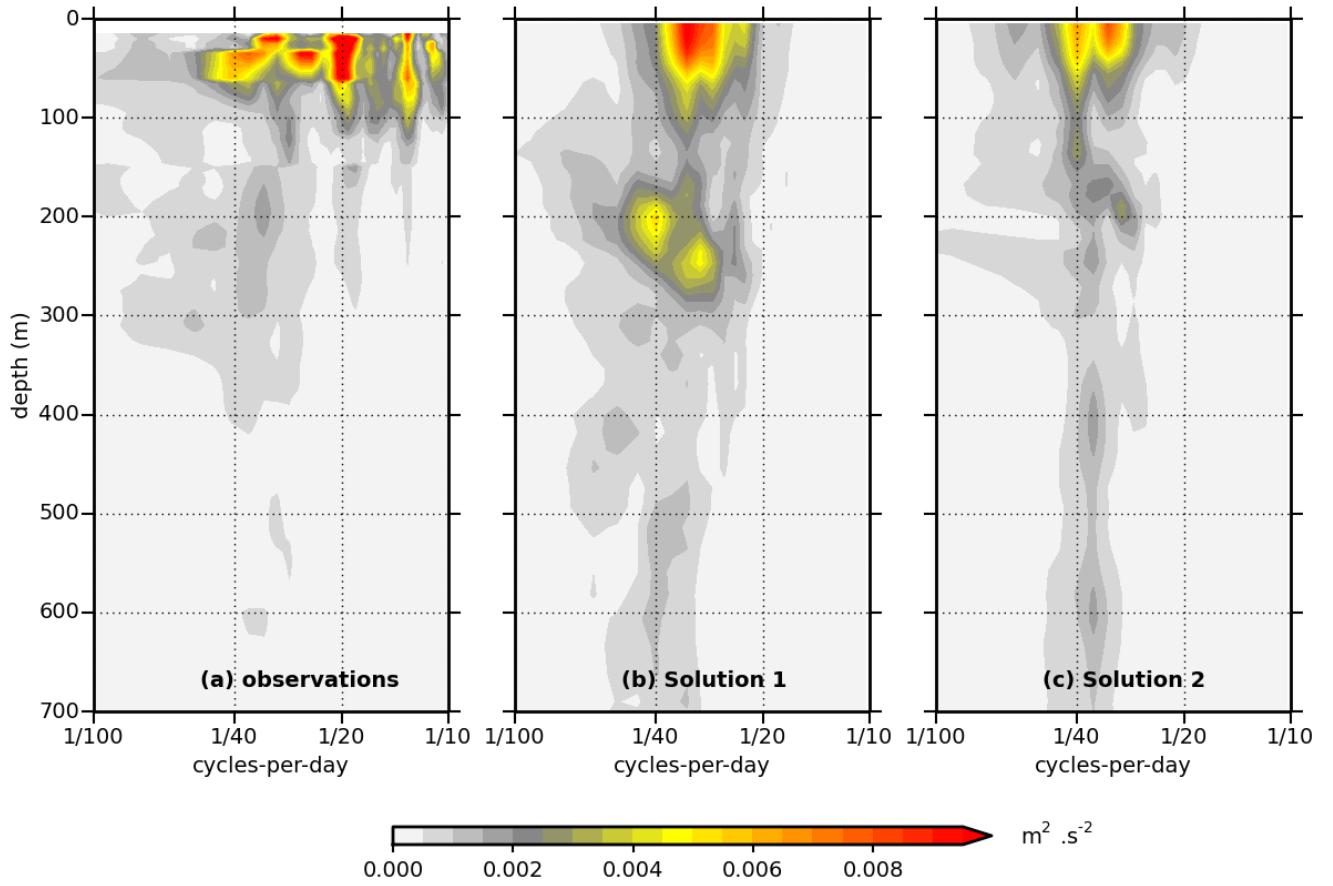


**Figure 8:** Variance-preserving power density spectra of equatorial  $v$  at  $23^\circ\text{W}$  in (a) observations, (b) Solution 1 and (c) Solution 2. Spectral calculations are identical to those of Fig. 7 except that they are performed at every available depth and only at  $23^\circ\text{W}$ . This results in 5.4 segments on average for each depth ( $dof=14$ ) for the observations, 8 segments per depth ( $dof=21$ ; years 24 to 31) for Solution 1 and 6 segments per depth ( $dof=16$ ; years 24 to 30) for Solution 2. The observations are those reported in Brandt *et al.* (2012; 10-year long coverage).

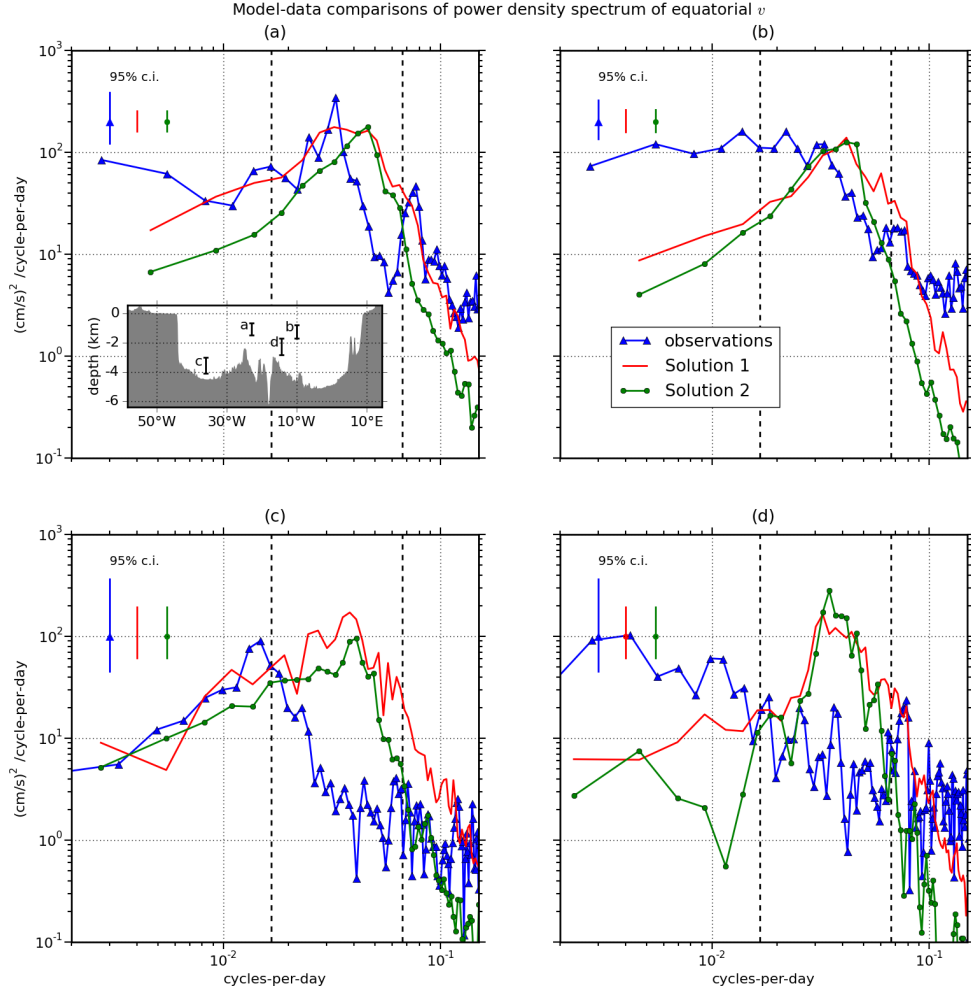


**Figure 9:** Model-data comparisons of power density spectrum of equatorial  $v$ : (blue) observations, (red) Solution 1 and (green) Solution 2. Spectral calculations are conducted as for the spectra of Fig. 7 except that to construct the model spectra, we average spectra from the depths and locations that are near the actual moorings and either one-year or 20-month long segments depending on the duration of the data: (a) observations at  $23^\circ\text{W}$  described in Bunge *et al.* (2008), a total of 9 one-year long segments ( $dof=32$ ) from 7 depths between 635 and 1486 m depth; (b) observations at  $10^\circ\text{W}$  also described in Bunge *et al.* (2008), a total of 15 one-year long segments ( $dof=40$ ) from 9 depths between 764 and 1689 m depth; (c) observations from the ACM10 mooring, a total of 3 20-month long segments ( $dof=8$ ) at 3, 3.6 and 4.1 km depth; and (d) observations from the ACM11 mooring, a total of 3 one-year long segments ( $dof=8$ ) at 1.7, 2 and 2.8 km depth. The longitude and depth range of each dataset is shown in the inlet panel in (a). Vertical dashed lines delimits the intraseasonal waveband (15-to-60-day period).

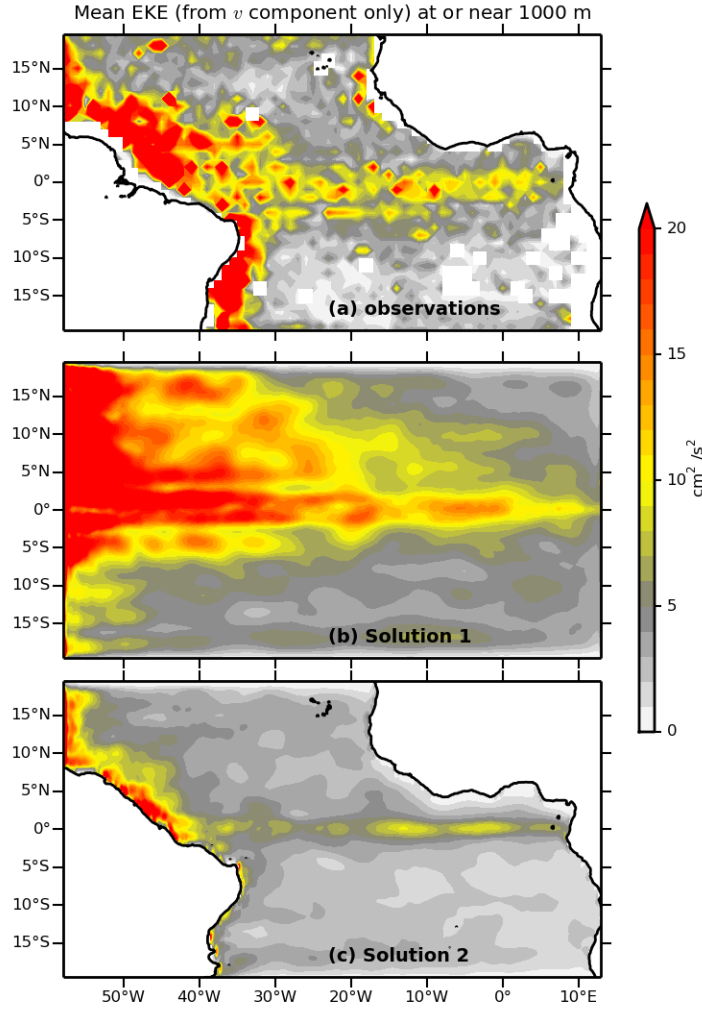


**Figure 10:** Mean EKE near 1000 m depth from the  $v$  component only (that is,  $1/2 \langle (v - \langle v \rangle)^2 \rangle$  where the angle brackets indicate the time average): (a) from Argo data as in Fig. 3 (panel b), (b) in Solution 1 and (c) in Solution 2. Average is over 1997-2014 for (a), and years 25 to 29 for (b) and (c). The model data have been low-pass filtered using a 10-day running mean before calculating the mean EKE in order to mimic the typical sampling scheme of the Argo data (about once every 10 days).

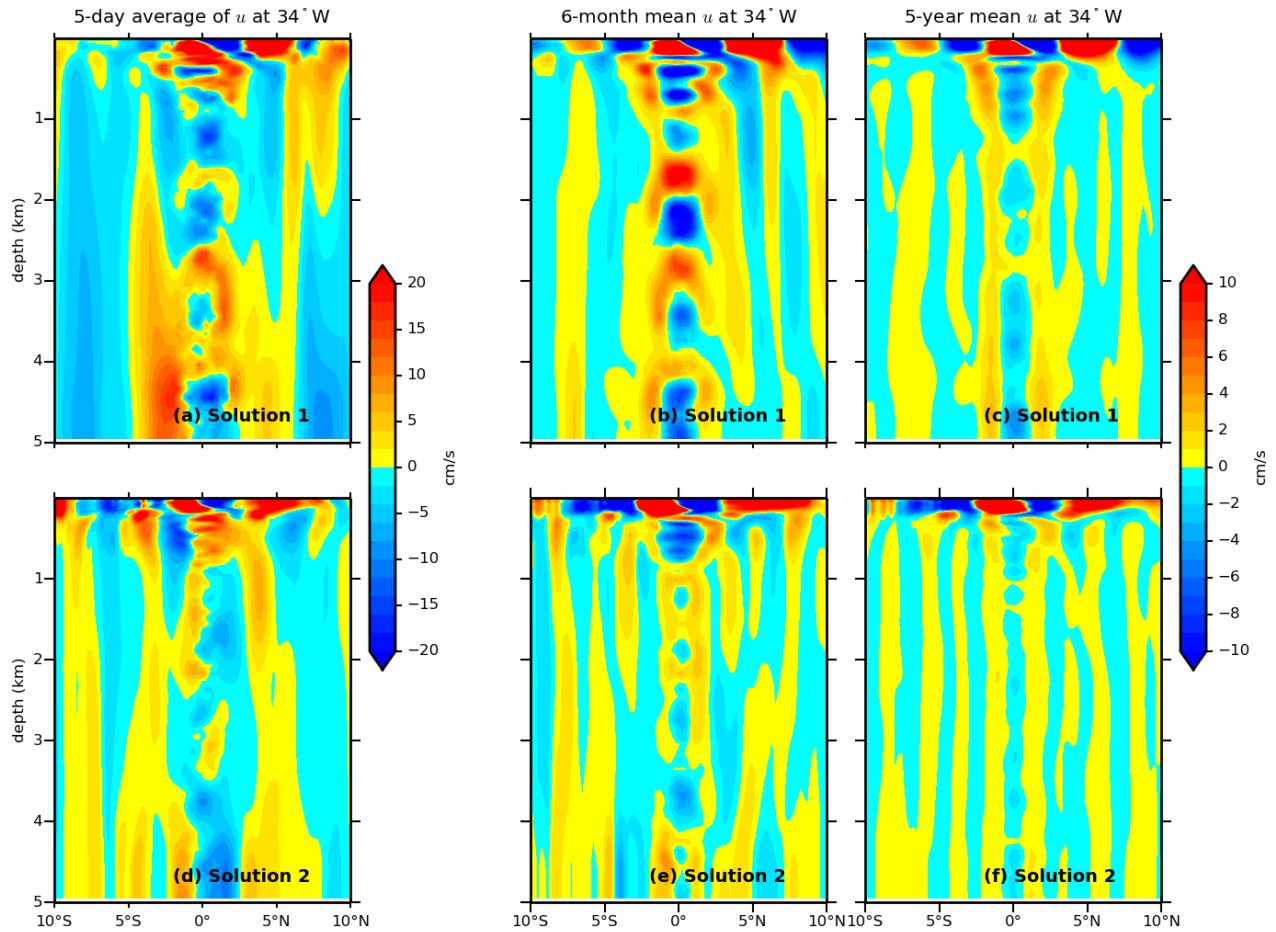


**Figure 11:** (left) 5-day mean, (middle) 6-month and (right) 5-year mean  $u$  at  $34^\circ\text{W}$  in (upper) Solution 1 and (lower) Solution 2. For both runs, the 5-day mean on June 1 of year 29, the second half of year 29 and years 25 to 29 are used for the 5-day averages, the 6-month mean and the 5-year mean, respectively. Notice the different color scale for the 5-day averages and for the 6-month and 5-year means.

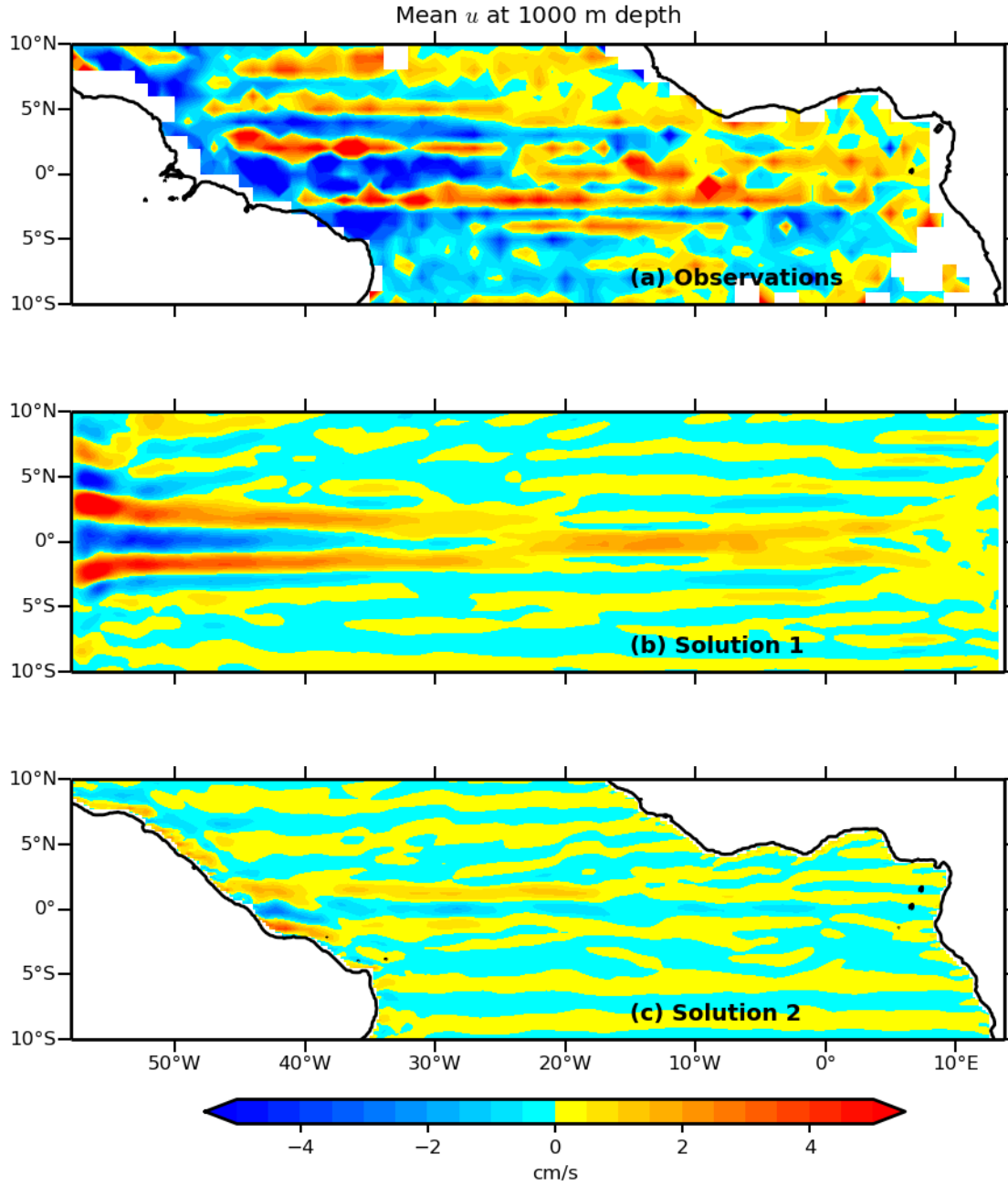


**Figure 12:** Mean  $u$  at 1000 m (upper) from Argo float displacements (see caption of Fig. 3) (middle) in Solution 1 and (lower) in Solution 2. Years 25 to 29 are used for Solution 1 and 2.

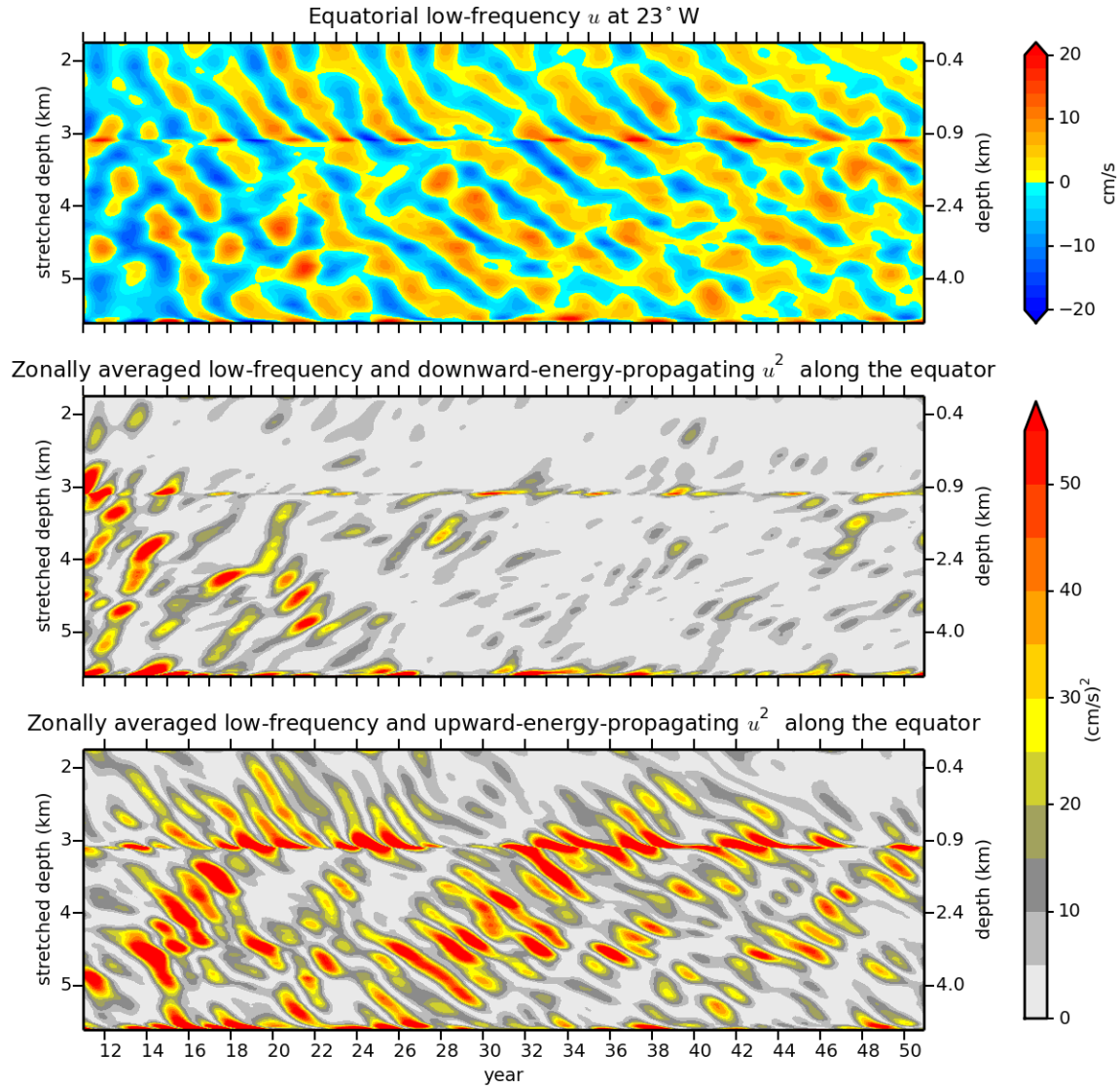


**Figure 13:** (upper) Time series of equatorial low-frequency (period  $> 1.75$  year)  $u$  at  $23^\circ$ W in Solution 1. Velocity profiles below 300 m have been vertically stretched and scaled (using a reference buoyancy frequency of 1 cph; Gill 1982) before being plotted; the stretched and unstretched depth ticks are shown on the left and right axes, respectively. In the middle and lower panels are plotted the squared amplitude averaged along the equator of the downward and upward energy propagating  $u$ , respectively. The anomalously high values near 3100 stretched meters depth in these two panels result from unrealistically weak stratification in the reference profile at this depth.

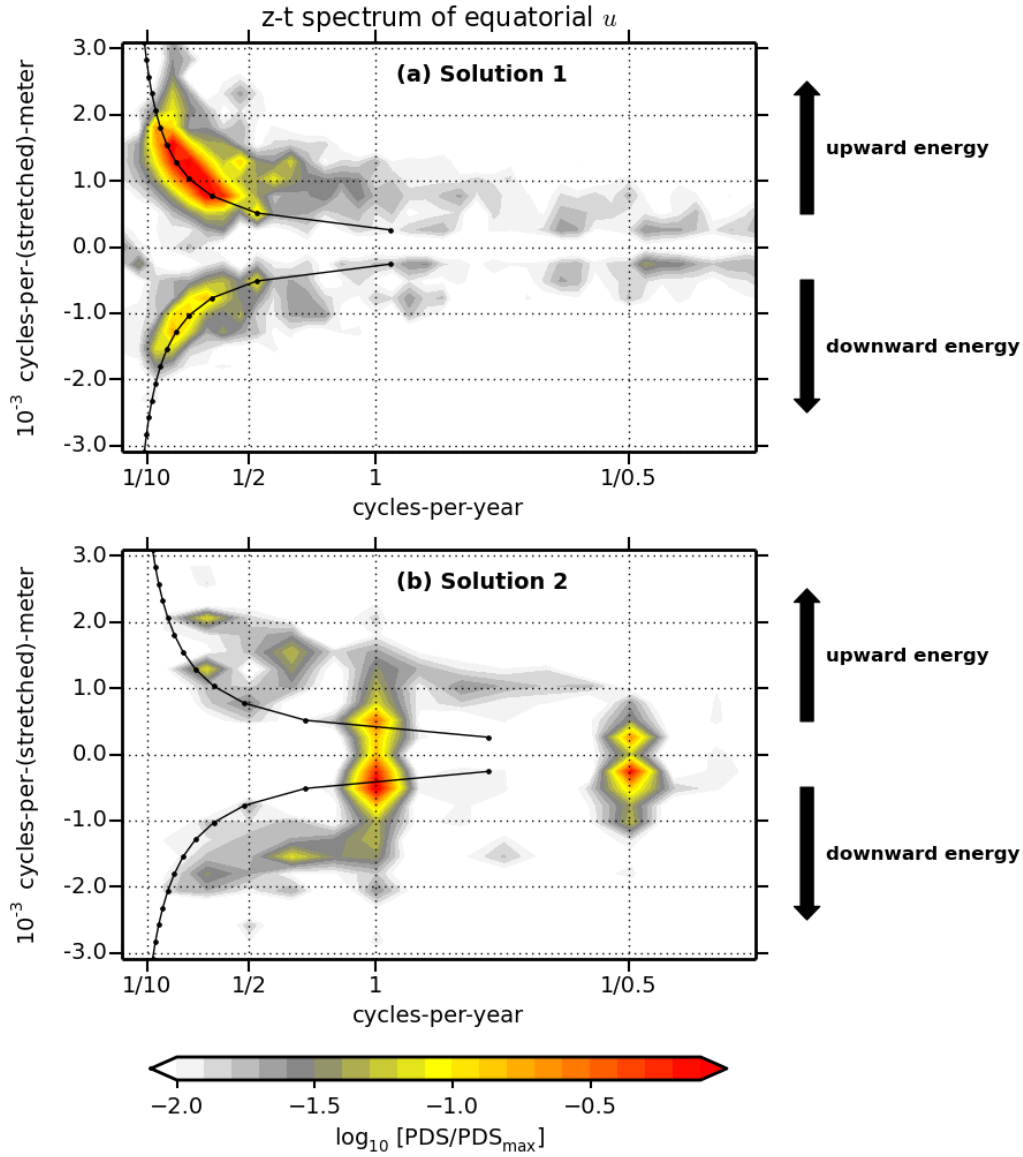


**Figure 14:** Spectrum of equatorial  $u$  in the frequency-vertical wavenumber space: (a) Solution 1 (years 10 to 49) and (b) Solution 2 (years 24 to 29). Each spectrum is the average of spectra calculated every  $2^\circ$  along the equator and is normalized by its maximum value before being plotted on a logarithmic scale. For Solution 1, the spectrum is computed from a set of 15-year time series shifted in time every 2.5 years; for Solution 2, the full time series between years 24 and 29 is used. Velocity profiles below 300 m are stretched and scaled as in Fig. 13 before computing the spectra. The dotted black lines show the distribution of energy expected for low-frequency baroclinic equatorial basin modes (Eq. (1); Cane and Moore 1981).

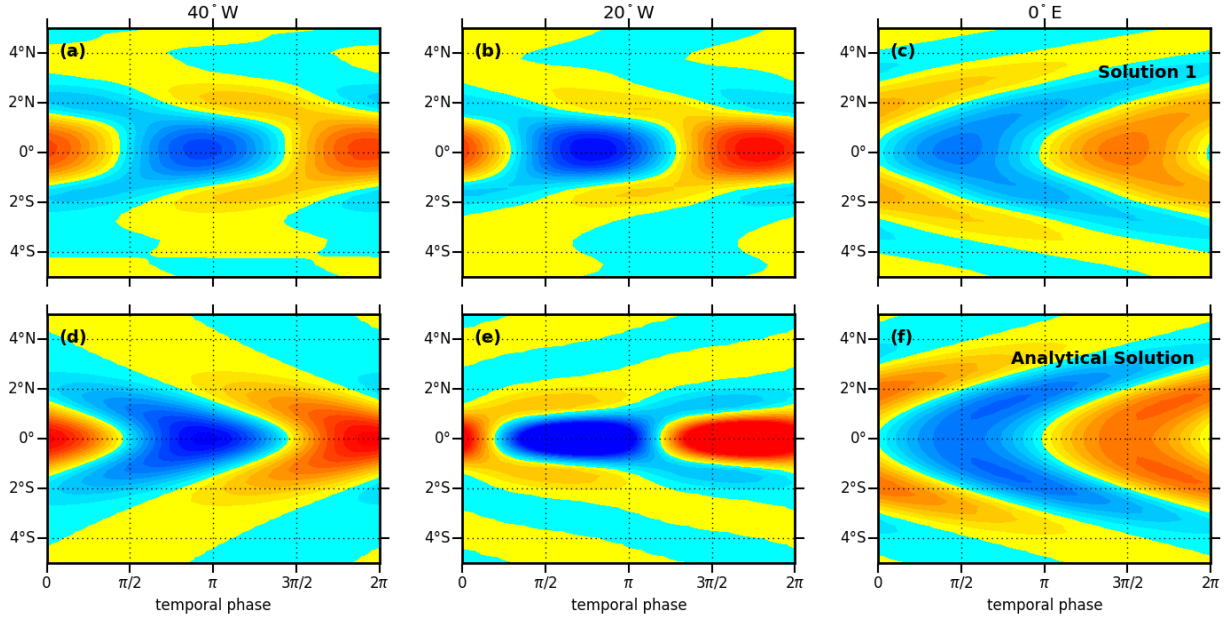


**Figure 15:** Meridional and temporal structure of upward-energy  $u$  at the 3.9-year period and 930 stretched meters vertical wavelength (vertical mode 12): (upper) from Solution 1 and (lower) from the theory of Cane and Moore (1981), with a Rayleigh damping coefficient  $r = r_0 \cdot [1, 2, \dots, l]$  that is linearly increasing with the absolute meridional mode number  $|l|$  with  $r_0 = 2 \times 10^{-9} \text{ s}^{-1}$ . The longitudes are (left)  $40^\circ\text{W}$ , (middle)  $20^\circ\text{W}$  and (right)  $0^\circ\text{E}$ . The abscissa is phase in radians over one period. The model and analytical solution have each been normalized by the maximum of its absolute value over the whole domain.



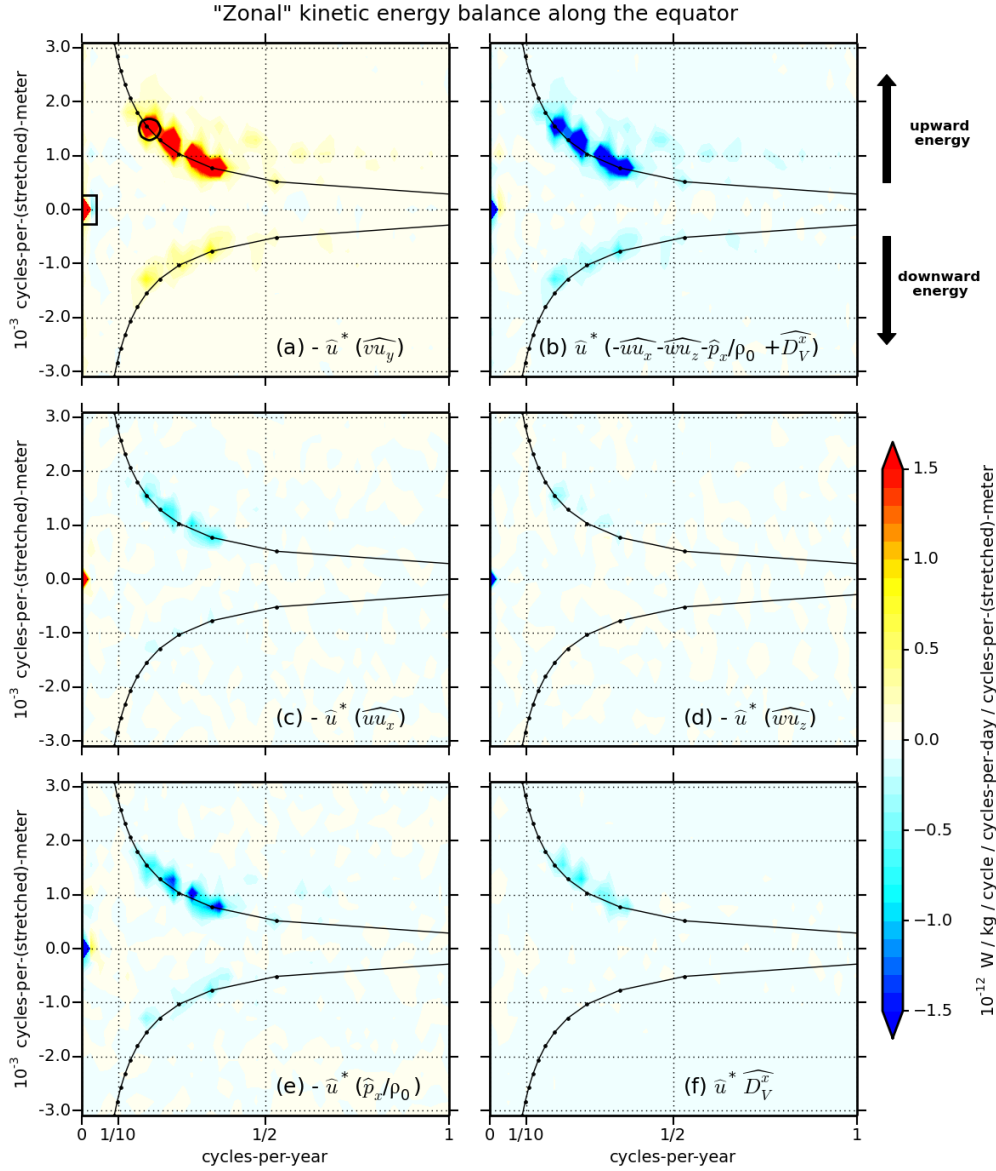


**Figure 16:** Zonal kinetic energy budget: Contribution to  $\partial_t u^2$  in the frequency-vertical wavenumber space by the real part of (a)  $-\hat{u}^* (\widehat{vu}_y)$ , (b)  $\hat{u}^* (-\widehat{uu}_x - \widehat{wu}_z - \widehat{p}_x/\rho_0 + \widehat{D}_V^x)$ , (c)  $-\hat{u}^* (\widehat{uu}_x)$ , (d)  $-\hat{u}^* (\widehat{wu}_z)$ , (e)  $-\hat{u}^* (\widehat{p}_x/\rho_0)$  and (f)  $\hat{u}^* \widehat{D}_V^x$  along the equator in Solution 1; see text for details. The term  $\hat{u}^* \widehat{D}_H^x$  is weak and is not shown. Velocities from years 10 to 49 and below 300 m are stretched and scaled as in Fig. 13 before computing the spectra. The spectra are calculated every  $2^\circ$  in longitude and then averaged. The small box in (a) corresponds to the LEIC that is the focus of Figs. 17, 18 and 19 while the circle marks a basin mode that composes the EDJs and is the focus of Fig. 20. The dotted black lines show the basin mode dispersion relation as in Fig. 14.

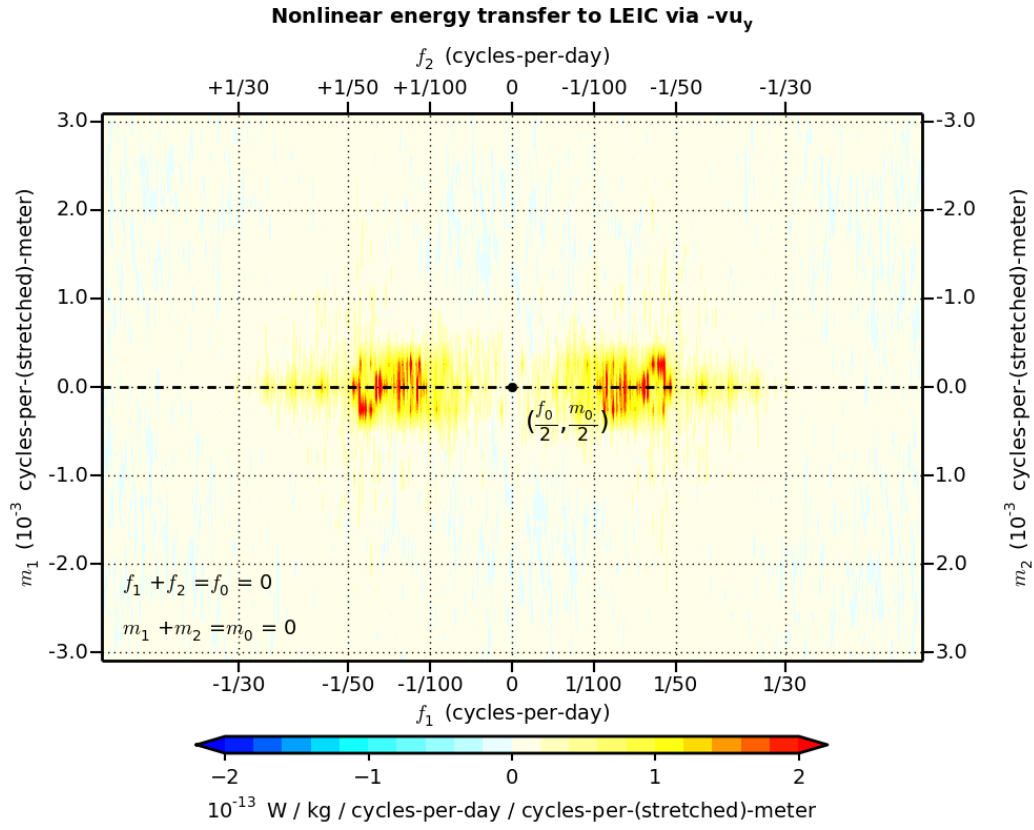


**Figure 17:** Nonlinear energy transfer (in frequency-vertical wavenumber space) to the LEIC ( $f_0=0$  and  $m_0=0$ ; square symbol in Fig. 16a) via the term  $-vu_y$  in Solution 1, that is quantity (5). Positive (red/yellow) values indicate a transfer of energy to LEIC and the reverse for negative values (blue/cyan).  $(f_i, m_i)$  are the frequency and wavenumber (in stretched vertical coordinate) of the wave  $i=1,2$ . Spectra are calculated as in Fig. 16 but for 20-year long segments with 50% overlap, then averaged.

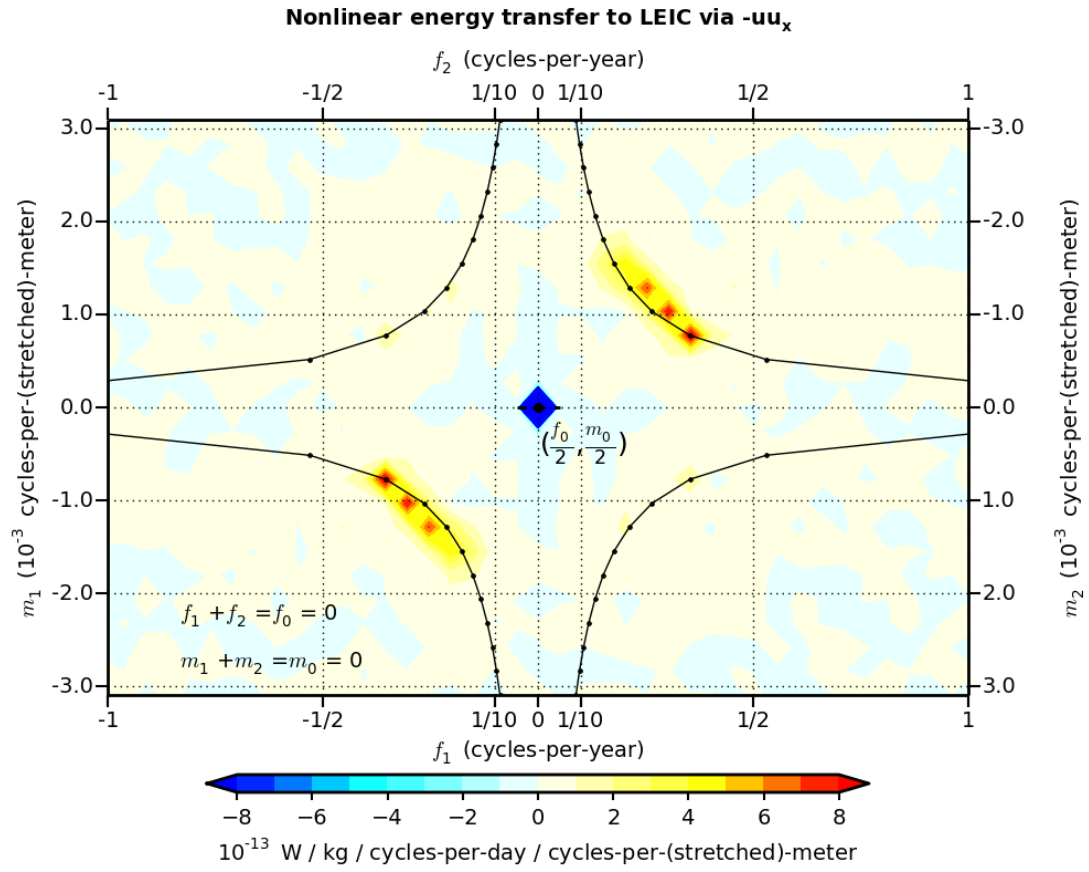


**Figure 18:** Nonlinear energy transfer (in frequency-vertical wavenumber space) to the LEIC ( $f_0=0$  and  $m_0=0$ ; square symbol in Fig. 16a) *via* the term  $-uu_x$  in Solution 1, that is quantity (6). See caption of Fig. 17 for details.

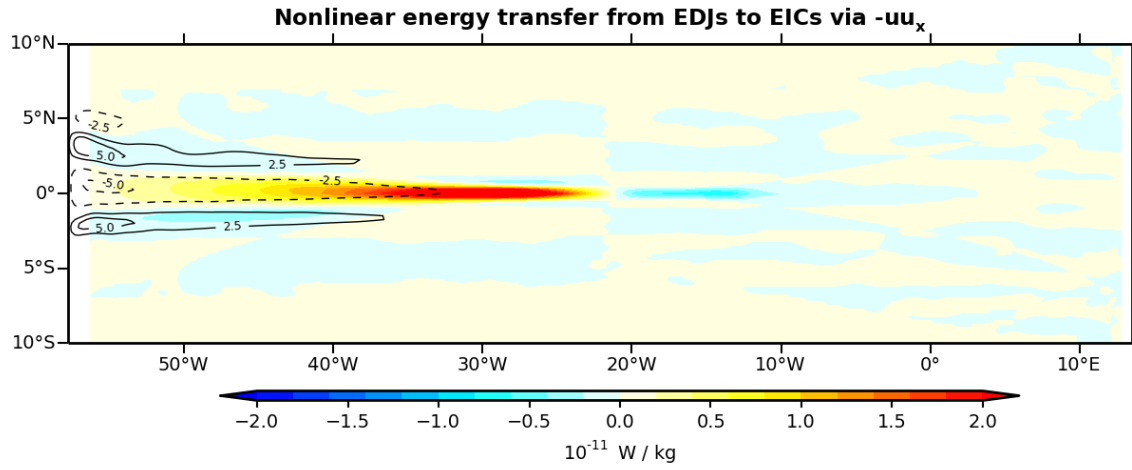


**Figure 19:** Nonlinear energy transfer (in physical space) from a particular EDJ basin mode to EICs *via* the term  $-uu_x$ , that is quantity (7). The EDJs used in this calculation correspond to the theoretical basin mode shown in the lower panels of Fig. 15 with a maximum amplitude of 10 cm/s, while the EICs are defined as the time and vertical averaged zonal velocity below 300 m from Solution 1 (years 25 to 29). Contours of EICs in cm/s are plotted in black.

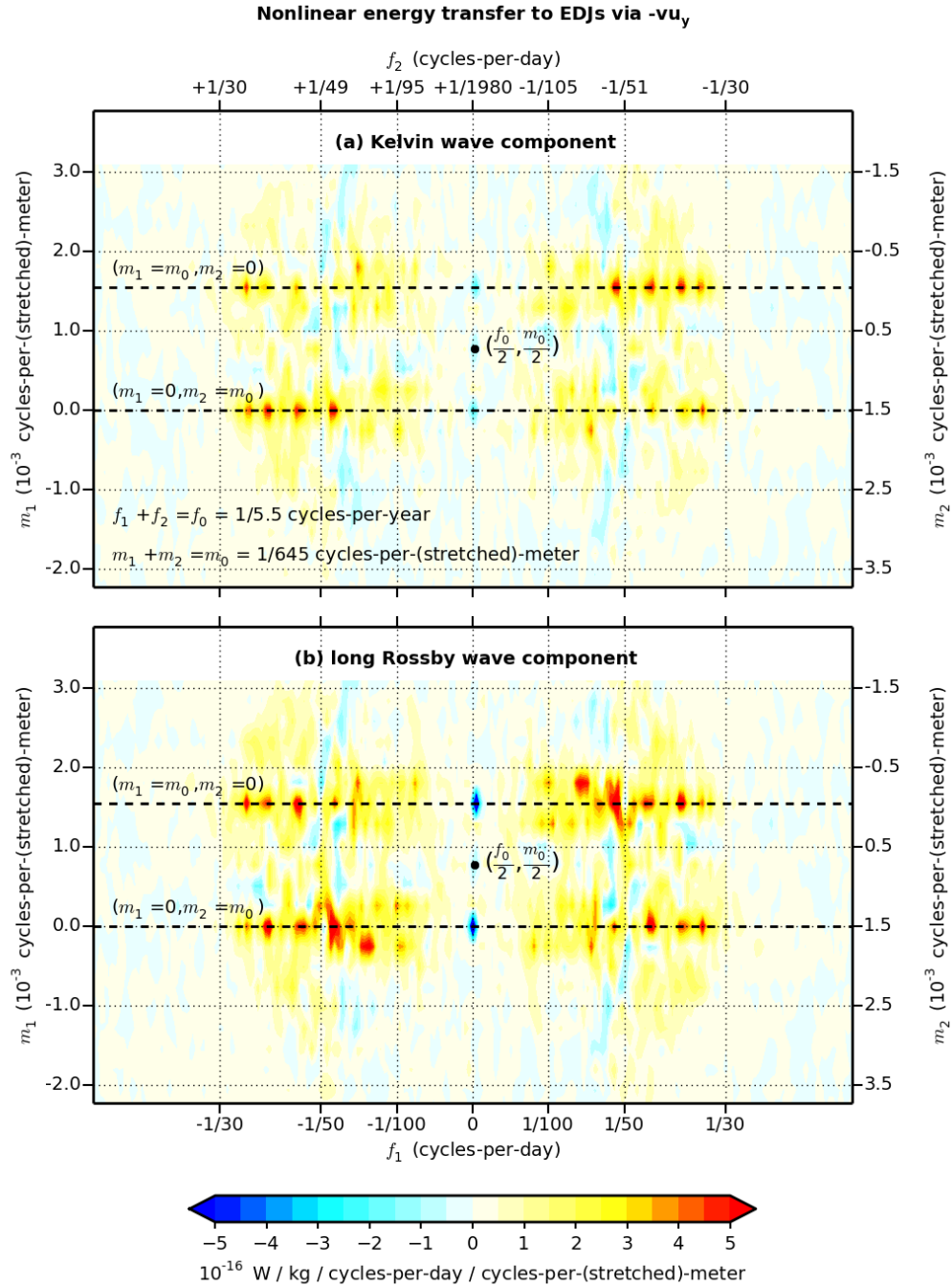


**Figure 20:** Nonlinear transfer of energy (in frequency-vertical wavenumber space) to (a) the Kelvin wave component – that is quantity (10) – and (b) long Rossby wave component – that is quantity (11) – of a particular EDJ basin mode ( $f_0=1/5.5$  cycles-per-year and  $m_0=1/645$  cycles-per-meter; circle symbol in Fig. 16a) via the nonlinear term  $-vu_y$  in Solution 1. The meaning of the color code is the same as in Fig. 17.  $(f_i, m_i)$  are the frequency and wavenumber (in stretched vertical coordinate) of the wave  $i=1,2$ . Spectra are calculated as in Fig. 16 but for 5.5-year long segments with 50% overlap then averaged.